Open Archive TOULOUSE Archive Ouverte (OATAO)

OATAO is an open access repository that collects the work of Toulouse researchers and makes it freely available over the web where possible.

Global bifurcations to subcritical magnetorotational dynamo action in Keplerian shear flow

A. RIOLS[1,2], F. RINCON[1,2] †, C. COSSU[3], G. LESUR[4], P.-Y. LONGARETTI[4], G. I. OGILVIE[5] and J. HERAULT[6]

[1]Université de Toulouse; UPS-OMP; IRAP; Toulouse, France

[2]CNRS; IRAP; 14 avenue Edouard Belin, F-31400 Toulouse, France

[3]CNRS-Institut de Mécanique des Fluides de Toulouse (IMFT), Allée du Professeur Camille Soula, 31400 Toulouse, France

[4]UJF-Grenoble 1 / CNRS-INSU, Institut de Planétologie et d'Astrophysique de Grenoble (IPAG) UMR 5274, Grenoble, F-38041, France

[5]Department of Applied Mathematics and Theoretical Physics, University of Cambridge, Centre for Mathematical Sciences, Wilberforce Road, Cambridge CB3 0WA, United Kingdom

[6]Laboratoire de Physique Statistique de l'Ecole Normale Supérieure, CNRS UMR 8550, 24 Rue Lhomond, 75231 Paris Cedex 05, France

Magnetorotational dynamo action in Keplerian shear flow is a three-dimensional, nonlinear magnetohydrodynamic process whose study is relevant to the understanding of accretion processes and magnetic field generation in astrophysics. Transition to this form of dynamo action is subcritical and shares many characteristics of transition to turbulence in non-rotating hydrodynamic shear flows. This suggests that these different fluid systems become active through similar generic bifurcation mechanisms, which in both cases have eluded detailed understanding so far. In this paper, we build on recent work on the two problems to investigate numerically the bifurcation mechanisms at work in the incompressible Keplerian magnetorotational dynamo problem in the shearing box framework. Using numerical techniques imported from dynamical systems research, we show that the onset of chaotic dynamo action at magnetic Prandtl numbers larger than unity is primarily associated with global homoclinic and heteroclinic bifurcations of nonlinear magnetorotational dynamo cycles. These global bifurcations are found to be supplemented by local bifurcations of cycles marking the beginning of period-doubling cascades. The results suggest that nonlinear magnetorotational dynamo cycles provide the pathway to turbulent injection of both kinetic and magnetic energy in incompressible magnetohydrodynamic Keplerian shear flow in the absence of an externally imposed magnetic field. Studying the nonlinear physics and bifurcations of these cycles in different regimes and configurations may subsequently help to better understand the physical conditions of excitation of magnetohydrodynamic turbulence and instability-driven dynamos in a variety of astrophysical systems and laboratory experiments. The detailed characterization of global bifurcations provided for this three-dimensional subcritical fluid dynamics problem may also prove useful for the problem of transition to turbulence in hydrodynamic shear flows.

† Email address for correspondence: francois.rincon@irap.omp.eu

1. Introduction

1.1. *Scientific context and motivations*

Magnetorotational dynamo action is a three-dimensional, nonlinear magnetohydrodynamic (MHD) process whose study is most directly relevant to the understanding of accretion processes and magnetic field generation in astrophysics. Accretion takes place in young stellar objects, interacting binary systems and galactic nuclei and is known in many cases to be mediated by a fluid disk (Pringle 1981; Papaloizou & Lin 1995; Lin & Papaloizou 1996; Frank *et al.* 2002; Hartmann 2009; Armitage 2010). Typical luminosity variation timescales inferred from observations of these systems indicate that they accrete at a fairly high rate, which requires that vertical angular momentum be efficiently transported outwards through the disk (Lynden-Bell & Pringle 1974). Identifying and characterizing efficient transport mechanisms in disks is one of the most important questions of astrophysical fluid dynamics (Balbus & Hawley 1998; Balbus 2003).

Turbulent transport is a most plausible candidate in this respect and is thought to be related to the nonlinear development of the magnetorotational instability (MRI), a linear MHD instability occurring in differentially rotating flows whose rotation rate Ω decreases with the distance to the rotation axis (Velikhov 1959; Chandrasekhar 1960; Balbus & Hawley 1991). Keplerian flow, $\Omega(r) \propto 1/r^{3/2}$, is the most studied MRI-unstable flow. The MRI draws energy from the background shear but requires the presence of a magnetic field $\boldsymbol{B}$, as the instability is mediated by magnetic tension. For instance, plane waves with a wavenumber $\boldsymbol{k}$ can only be MRI-unstable if $\boldsymbol{k} \cdot \boldsymbol{B} \neq 0$. In the presence of a uniform background magnetic field threading the flow, the MRI acts as a genuine linear instability which proceeds exponentially in time and breaks down into MHD turbulence in both two and three dimensions (Hawley & Balbus 1991; Hawley *et al.* 1995). How efficient this turbulence is at transporting angular momentum remains a matter of debate (Fromang & Papaloizou 2007; Lesur & Longaretti 2007; Longaretti & Lesur 2010) and may significantly depend on the physical characteristics of the disk plasma, such as its magnetic Prandtl number Pm (Balbus & Henri 2008). Another important issue is that this simple configuration is probably not relevant to all kinds of accreting systems. In the absence of an externally imposed field (henceforth referred to as a zero net-flux configuration), one may wonder whether MRI-driven MHD turbulence can be sustained at all in disks. For this to be possible, vigorous magnetic induction must be present to sustain a zero net-flux, MRI-mediating field against ohmic diffusion, but the Keplerian flow itself is not a dynamo. One possibility is that the field is sustained by the MRI-driven turbulence itself, leading to a dynamo in which magnetic field generation and turbulence activation processes are intrinsically coupled. This is the MRI *dynamo* problem.

Early numerical simulations indicated that this form of dynamo can indeed be excited in Keplerian flow, but only in three dimensions (as expected from Cowling's anti-dynamo theorem), only for initial perturbations of finite amplitude, and only if the dynamical effects of the magnetic field on the flow (magnetic tension) are taken into account (Brandenburg *et al.* 1995; Hawley *et al.* 1996). The latter requirements clearly suggest that some form of MRI is active in the process and that the dynamo is not kinematic. This built-in nonlinearity is one of the main reasons why it has so far proven very difficult to understand the dynamo transition even qualitatively. In particular, the very existence of an MRI dynamo mechanism at low Pm (the most common dissipative regime in disks) remains a widely debated issue (Fromang *et al.* 2007; Davis *et al.* 2010; Bodo *et al.* 2011; Käpylä & Korpi 2011; Simon *et al.* 2011; Oishi & Mac Low 2011).

The MRI dynamo actually provides a clear illustration of a whole class of subcritical dynamos in (possibly rotating) shear flows prone to MHD instabilities, sometimes

referred to as instability-driven dynamos (e. g. Spruit 2002; Cline *et al.* 2003; Rincon *et al.* 2008). These dynamos are very interesting from the astrophysical point of view because they seem to naturally generate time-dependent, system-scale coherent magnetic fields but appear to be different in nature from all kinds of linear kinematic dynamos commonly invoked in the astrophysical context (Brandenburg *et al.* 1995), such as the mean-field (Steenbeck *et al.* 1966; Moffatt 1977) and fluctuation (turbulent, small-scale) dynamos (Zel'dovich *et al.* 1984; Childress & Gilbert 1995). The MRI dynamo is also a good candidate for detection in laboratory experiments, which makes it a particularly worthwhile object of study in the broader context of dynamo theory.

Uncovering the exact bifurcation mechanisms underlying the MRI dynamo transition has not yet proven possible but is clearly an essential prerequisite to making progress on a variety of astrophysical and MHD problems. The objective of this paper is to address this transition problem from a fundamental fluid dynamics perspective, mostly leaving aside astrophysical applications. As will be explained in detail shortly, the problem is actually similar to that of hydrodynamic transition to turbulence of non-rotating linearly stable shear flows, about which much has been learned in recent years. The approach taken on in this paper is based on the assumption that similar progress on the MRI dynamo problem may be possible along the same lines. To motivate this approach, we find it useful to offer a short summary of the status of research on hydrodynamic shear flows in the next paragraph. Readers familiar with the problem may jump directly to §1.3, where the connections with the MRI dynamo are explained in detail.

1.2. *Hydrodynamic transition in shear flows*

The origins of hydrodynamic turbulence in linearly stable non-rotating shear flows is a long-standing problem (Reynolds 1883) which has been extensively reviewed (Grossmann 2000; Kerswell 2005; Eckhardt *et al.* 2007; Eckhardt 2009; Kawahara *et al.* 2012). Transition in such flows is known both experimentally and numerically to be subcritical (Darbyshire & Mullin 1995; Dauchot & Daviaud 1995*a*; Hof *et al.* 2003), and numerical and theoretical work conducted in the 1990s indicated that the transitional dynamics relies on a nonlinear hydrodynamic self-sustaining process (SSP) (Hamilton *et al.* 1995; Waleffe 1995*a,b*, 1997). Let us denote the direction aligned with the base flow as the streamwise direction. The self-sustaining process, illustrated in figure 1 (left), consists in an interplay between non-normal transient amplification of streamwise-independent velocity structures (the so-called streaks) by the lift-up mechanism acting on weak streamwise-independent streamwise vortices (Landahl 1980; Schmid & Henningson 2000; Dauchot & Daviaud 1995*b*), and streamwise-dependent unstable perturbations of the streaks. These perturbations feed back nonlinearly on the streamwise vortices, making it possible for the flow as a whole to be self-sustaining (Waleffe 1995*b*). This mechanism is believed to be active even in fully developed turbulent flows (Hwang & Cossu 2010, 2011).

Another characteristic of hydrodynamic shear flow turbulence in many laboratory and numerical experiments is its transient nature, which suggests that the transitional dynamics is structured around a chaotic saddle, at least in constrained geometries† (Faisst & Eckhardt 2004; Kerswell 2005; Hof *et al.* 2006; Peixinho & Mullin 2006; Willis & Kerswell 2007; Hof *et al.* 2008; Schneider & Eckhardt 2008). The border in phase space separating initial conditions leading to rapid relaminarization of the flow from initial conditions leading to longer lived (but still ultimately decaying) chaotic states is a complicated surface commonly referred to as the "edge of chaos", on which flow trajectories

---

† The situation may be different in spatially extended systems in which spatiotemporal chaos can develop, see discussion in §7.4.
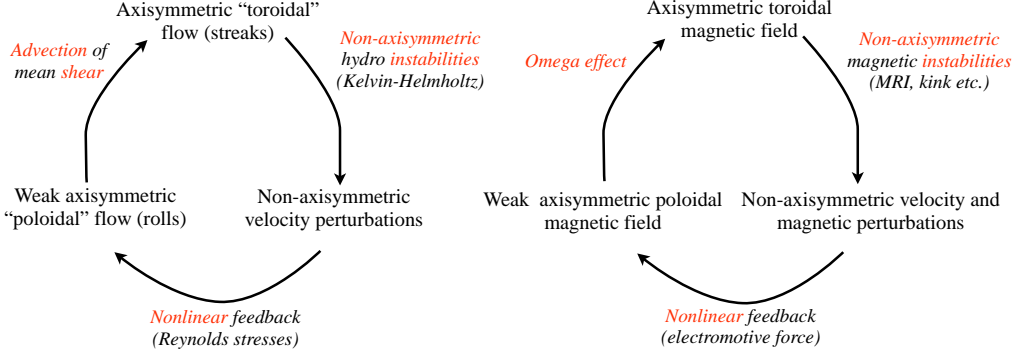
FIGURE 1. Hydrodynamic self-sustaining process (Waleffe 1997) and self-sustaining dynamo processes in shear flows prone to MHD instabilities (Rincon *et al.* 2007, 2008).

seem to converge to a relative fractal attractor. (Schmiegel 1997; Moehlis *et al.* 2004*a*,*b*; Skufca *et al.* 2006; Schneider *et al.* 2006, 2007*a*; Eckhardt *et al.* 2007; Willis & Kerswell 2007; Schneider *et al.* 2008; Kim & Moehlis 2008; Duguet *et al.* 2008*b*; Eckhardt 2009; Mellibovsky *et al.* 2009; Vollmer *et al.* 2009; de Lozar *et al.* 2012).

The causes of the transition have mostly been investigated using direct numerical simulations of reduced dynamical models (Moehlis *et al.* 2002, 2005; Vollmer *et al.* 2009; Lebovitz 2009, 2012), of pipe flow (Schneider *et al.* 2007*b*; Kerswell & Tutty 2007; Duguet *et al.* 2008*a*,*b*; Willis & Kerswell 2009; Mellibovsky & Eckhardt 2011, 2012; Willis *et al.* 2013) and of plane Couette flow (Wang *et al.* 2007; Gibson *et al.* 2008; Halcrow *et al.* 2009; van Veen & Kawahara 2011; Kreilos & Eckhardt 2012). Simple, three-dimensional nonlinear invariant solutions (fixed points, travelling waves, periodic and relative periodic orbits) of the Navier-Stokes equations whose dynamics relies on the self-sustaining process seem to play a critical role in the transition (Nagata 1990; Waleffe 1998, 2001; Itano & Toh 2001; Kawahara & Kida 2001; Waleffe 2003; Faisst & Eckhardt 2003; Hof *et al.* 2004; Wedin & Kerswell 2004; Pringle & Kerswell 2007; Viswanath 2007; Duguet *et al.* 2008*a*; Gibson *et al.* 2008, 2009; Pringle *et al.* 2009). However, a detailed understanding of the underlying bifurcation mechanisms and of how these solutions relate to the edge of chaos is still lacking. One of the most favoured hypotheses put forward by Schmiegel (1997) is the occurrence of chaos-generating global bifurcations involving the stable and unstable manifolds of such invariant "edge states". Indirect evidence for such bifurcations in the form of homoclinic and heteroclinic orbits has only recently been reported in plane Couette flow (Gibson *et al.* 2008; Halcrow *et al.* 2009; van Veen & Kawahara 2011). The most direct numerical evidence so far (Kreilos & Eckhardt 2012) suggests that both local (period-doubling cascades) and global bifurcations (boundary crises, see Grebogi *et al.* 1987; Ott 2002) may be important, but the field remains a very active area of research.

1.3. *Self-sustaining dynamo processes, transition and invariant solutions*

The idea that the MRI dynamo could be based on an analogous self-sustaining dynamo process was put forward by Rincon *et al.* (2007). Let us introduce some terminology to explain the analogy in detail. In dynamo theory, the shearwise and spanwise projections of vector fields are usually referred to as their poloidal components and their streamwise projection as their toroidal component. "Streamwise-independent" fields are

often referred to as "axisymmetric" fields in dynamo theory (even in cartesian coordinate systems), while "streamwise-dependent" translates into "non-axisymmetric".

The self-sustaining MRI dynamo process is illustrated in figure 1 (right). The first part is the stretching by the differential rotation of a weak, zero net-flux axisymmetric poloidal magnetic field into a stronger axisymmetric toroidal field. This so-called Ω effect is the analogue of the lift-up mechanism. The second part of the dynamo SSP is the amplification of non-axisymmetric perturbations by the MRI (Balbus & Hawley 1992; Ogilvie & Pringle 1996; Terquem & Papaloizou 1996; Brandenburg & Dintrans 2006; Lesur & Ogilvie 2008a). Recall that magnetic tension is essential to the MRI. A non-axisymmetric version of the instability is naturally expected in the presence of a dominant toroidal axisymmetric magnetic field, which is just what the Ω effect produces. The non-axisymmetric MRI of a toroidal field is the analogue in the dynamo SSP of the streamwise-dependent unstable perturbations of the streaks in the hydrodynamic SSP. The dynamo loop is closed thanks to the nonlinear interactions of MRI-amplified perturbations feeding back on the original axisymmetric field components through a nonlinear induction term (Lesur & Ogilvie 2008a,b). This is the dynamo equivalent of the nonlinear self-advection of streamwise-dependent unstable perturbations feeding back on streamwise vortices in the hydrodynamic problem. This scenario may also be relevant to dynamos involving other MHD instabilities (Rincon et al. 2008), such as the kink instability (Spruit 2002), magnetic buoyancy coupled to Kelvin-Helmholtz instability (Cline et al. 2003; Davies & Hughes 2011; Tobias et al. 2011), and magnetoshear instabilities (Miesch et al. 2007).

Recurrent forms of MRI dynamo action analogous to hydrodynamic regeneration cycles in non-rotating shear flows have been spotted in many simulations (Brandenburg et al. 1995; Stone et al. 1996; Lesur & Ogilvie 2008b; Gressel 2010; Davis et al. 2010; Simon et al. 2012), and incompressible MRI dynamo turbulence has also been found numerically to be supertransient (Rempel et al. 2010). A steady nonlinear three-dimensional MRI dynamo solution was computed in Keplerian plane Couette flow by Rincon et al. (2007) along the lines of homotopy-based computations of nonlinear solutions in hydrodynamic shear flows (Nagata 1990; Waleffe 2003; Wedin & Kerswell 2004), and an unstable nonlinear MRI dynamo periodic orbit (cycle) was recently discovered by Herault et al. (2011) in the shearing box numerical framework (see §2). Looking back at §1.2, investigating the role of such invariant solutions in the MRI dynamo transition appears to be the next logical step to make progress on the problem. This is the precise purpose of this work.

1.4. *Outline of the paper*

The framework of the study is introduced in §2. Section 3 is devoted to a direct numerical simulations exploration of the dynamo transition aiming at identifying the imprint of invariant solutions. Section 4 describes the numerical continuation and local stability analysis of several nonlinear MRI dynamo cycles spotted in the transitional regime and discusses a possible period-doubling route to chaos. A more direct transition scenario is put forward in §5, where a detailed characterization of chaos-generating global homoclinic and heteroclinic bifurcations associated with dynamo cycles is presented. A direct illustration of their connections with the transition described in §3 is finally provided in §6. Section 7 summarizes the main results and discusses their relevance to astrophysics, dynamo theory and shear flow turbulence, as well as some directions for future work.

2. Equations and numerical framework

The theoretical and numerical framework are the same as in earlier work by our group (Herault et al. 2011). The problem geometry, equations, and symmetry reductions are
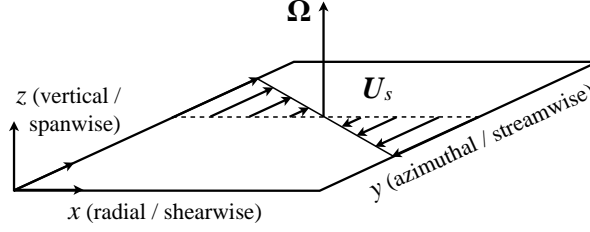
FIGURE 2. The Keplerian shearing sheet.

reproduced in this section for completeness, together with a few new notations and several important technical comments. We also discuss the numerical resolution and choices of system parameters. The numerical methods are described in detail in three appendices.

2.1. *The shearing sheet*

We use the shearing sheet description of differentially rotating flows (Goldreich & Lynden-Bell 1965), whereby an axisymmetric differential rotation profile is approximated locally by a linear shear flow $\boldsymbol{U}_s = -Sx\,\boldsymbol{e}_y$ and a uniform rotation rate $\boldsymbol{\Omega} = \Omega\,\boldsymbol{e}_z$ (figure 2). For a Keplerian flow, $\Omega = (2/3)\,S$. Here, (x, y, z) are respectively the shearwise, streamwise and spanwise directions (radial, azimuthal and vertical in accretion disks). To comply with dynamo terminology, we refer to the (x, z) projection of vector fields as their poloidal component and to their y projection as their toroidal component. "Axisymmetric" fields have no y dependence. Non-axisymmetric perturbations are usually referred to as "streamwise-dependent" perturbations in plane Couette flow. We consider incompressible velocity perturbations $\boldsymbol{u}$ and a magnetic field $\boldsymbol{B}$ which evolve according to the three-dimensional dissipative MHD equations in an unstratified shearing sheet:

$$\frac{\partial \boldsymbol{u}}{\partial t} - Sx\,\frac{\partial \boldsymbol{u}}{\partial y} + \boldsymbol{u} \cdot \boldsymbol{\nabla}\,\boldsymbol{u} = -2\,\boldsymbol{\Omega} \times \boldsymbol{u} + S\,u_x\,\boldsymbol{e}_y - \boldsymbol{\nabla}\,\Pi$$
$$+ \boldsymbol{B} \cdot \boldsymbol{\nabla}\boldsymbol{B} + \nu\Delta\,\boldsymbol{u}\,, \tag{2.1}$$

$$\frac{\partial \boldsymbol{B}}{\partial t} - Sx\,\frac{\partial \boldsymbol{B}}{\partial y} = -SB_x\,\boldsymbol{e}_y + \boldsymbol{\nabla} \times (\boldsymbol{u} \times \boldsymbol{B}) + \eta\Delta\boldsymbol{B}\,, \tag{2.2}$$

$$\boldsymbol{\nabla} \cdot \boldsymbol{u} = 0\,, \quad \boldsymbol{\nabla} \cdot \boldsymbol{B} = 0\,. \tag{2.3}$$

The kinetic and magnetic Reynolds numbers are defined by $Re = SL^2/\nu$ and $Rm = SL^2/\eta$, where ν and η are the constant kinematic viscosity and magnetic diffusivity, L is a typical scale of the spatial domain considered and time is measured with respect to S^{-1}. We also introduce the magnetic Prandtl number, $Pm = \nu/\eta$. Π is the total pressure (including magnetic pressure) divided by the uniform density. $\boldsymbol{B}$ is expressed as an equivalent Alfvén velocity and both $\boldsymbol{u}$ and $\boldsymbol{B}$ are measured with respect to SL.

2.2. *Large-scale dynamo equation: the critical role of Rm*

The fundamentals of self-sustaining dynamo processes introduced qualitatively in §1.3 can be described in mathematical terms using a "large-scale dynamo equation" obtained by averaging equation (2.2) over y:

$$\frac{\partial \overline{\boldsymbol{B}}}{\partial t} = -S\overline{B}_x\boldsymbol{e}_y + \overline{\boldsymbol{\nabla} \times \boldsymbol{\mathcal{E}}} + \eta\Delta\overline{\boldsymbol{B}}\,, \tag{2.4}$$

where the overline denotes an average along the y direction and $\overline{\boldsymbol{B}} = \overline{\boldsymbol{B}}(x, z, t)$ only. The first term on the r.h.s. describes the stretching of the axisymmetric (streamwise-

independent) poloidal magnetic field into a toroidal component. The second term is a magnetic induction term which involves the axisymmetric projection $\overline{\mathcal{E}}$ of an electromotive force (EMF) $\mathcal{E} = \boldsymbol{u} \times \boldsymbol{B}$ generated by the nonlinear couplings between velocity and magnetic perturbations. In the MRI dynamo SSP, this EMF is the nonlinear outcome of the transient development of a non-axisymmetric MRI and drives large-scale field reversals (Herault *et al.* 2011). The third term represents resistive damping. The presence of this term in the dynamo equation makes the magnetic Reynolds number Rm a most important parameter of the problem. Equation (2.4) is the equivalent in the MRI dynamo problem of the equation for streamwise vortices and streaks in the hydrodynamic shear flow problem, with the lift-up term replaced by the Ω effect term, the nonlinear advection term replaced by the induction term, and the viscous term proportional to $1/Re$ replaced by the magnetic diffusion term proportional to $1/Rm$. Viscous dissipation is of course part of the full problem, but does not appear explicitly in equation (2.4).

2.3. *Symmetries*

Enforcing symmetries is helpful to reduce the dynamics to lower-dimensional subspaces and therefore makes it easier to understand. Nagata (1986) identified several symmetries for three-dimensional nonlinear hydrodynamic solutions in Taylor-Couette flow in the thin-gap limit, equivalent to a wall-bounded cartesian plane Couette flow rotating about its spanwise z axis. Similar symmetries exist for MHD flows in the shearing sheet. Herault *et al.* (2011) showed that nonlinear states approaching a symmetry labelled $\mathcal{A}_1$ in analogy with Nagata's work are regularly excited in the MRI dynamo problem in the numerical configurations used in this paper. The mathematical description of this symmetry is repeated in appendix A.4. We will mostly investigate the dynamics in that subspace and will show in §3 that this restriction does not compromise the underlying fundamental complexity of the problem. Appropriate conjugation relations between Fourier modes must be imposed throughout the numerical time integrations to enforce the symmetry and eliminate the growth of non-symmetric perturbations seeded by numerical noise. We will notably monitor the fundamental Fourier mode in z of $\overline{\boldsymbol{B}}$, defined as

$$\overline{\boldsymbol{B}}_0(z,t) = \overline{\boldsymbol{B}}_0(t) \cos\left(\frac{2\pi}{L_z}\,z\right), \qquad (2.5)$$

as this mode is always and by a large amount the dominant contribution to the total axisymmetric magnetic field when the dynamics takes place in the symmetric $\mathcal{A}_1$ subspace.

2.4. *Numerical methods*

The numerics are based on a spectral version of the so-called shearing box model, which is a numerical implementation of equations (2.1)-(2.3) in a finite numerical domain. We use two complementary techniques to investigate the dynamics. The first one, direct numerical simulation (DNS), is used to integrate the equations in time starting from various initial conditions. The second one, Newton iteration, is used to compute accurate numerical representations of remarkable solutions such as nonlinear cycles.

2.4.1. *Direct numerical simulations in the shearing box*

DNS are carried out in the Keplerian shearing box with the SNOOPY code (Lesur & Longaretti 2007) in a domain of size (L_x, L_y, L_z), at numerical resolution (N_x, N_y, N_z). Let us summarize the important qualitative features of the model (see appendix A for details). The y and z directions are taken as periodic, while a so-called shear periodicity is assumed in the x direction. The latter amounts to assuming that a linear shear flow is constantly imposed and that all quantities are periodic in all spatial directions in a

sheared Lagrangian frame. A discrete spectral basis of "shearing waves" with constant k_y and k_z wavenumbers and constant shearwise Lagrangian wavenumber k'_x is used to represent fields in the sheared Lagrangian frame. A pseudo-spectral method with dealiasing is used to compute the nonlinear terms. The time integration scheme is a first order operator splitting method coupling an explicit third-order Runge-Kutta algorithm for the ideal MHD terms and an implicit exact scheme for the dissipative terms.

Hydrodynamic turbulence and transport in shear flows have been widely studied in such homogeneous shear flow simulations (Pumir 1996; Gualtieri *et al.* 2002; Casciola *et al.* 2003). The most notable difference with wall-bounded plane Couette flow is the nonlinear feedback on the background shear, which vanishes on average (in time) in the shearing box. The absence of walls may also at first glance suggest that important effects such as wave reflections are missing, but a physical nonlinear scattering mechanism of non-axisymmetric shearing waves mediated by the radial (shearwise) modulation of the axisymmetric (streamwise-independent) projections of the fields is actually present in the system (Herault *et al.* 2011).

2.4.2. *Newton-Krylov algorithm*

Newton's method is a standard tool of nonlinear analysis which has proven most useful for computing simple nonlinear hydrodynamic solutions in shear flows (see §1.2 and §1.3). The most powerful and memory-saving methods to perform the algebra in such high-dimensional systems (of typical size 10 000 or larger) involving dense Jacobians are iterative methods such as Krylov iteration. We developed our own Newton-Krylov solver PEANUTS for the MRI dynamo problem along the lines described by Viswanath (2007). The solver is based on the PETSc toolkit (Balay *et al.* 2011) and can be interfaced with different time-integrators to compute nonlinear equilibria, travelling waves and periodic/relative periodic orbits for a variety of partial differential equations. The iterative GMRES algorithm is used to solve the linear Jacobian system at each Newton iteration. For a nonlinear cycle search, the code attempts to minimize $||\boldsymbol{X}(T) - \boldsymbol{X}(0)||_2/||\boldsymbol{X}(0)||_2$, where $\boldsymbol{X}(t)$ is a state vector containing all independent field components at time t, and T is a guess for the period. The solver also performs pseudo-arclength continuation of nonlinear solutions with respect to any relevant system parameter and computes their local stability properties with an iterative Arnoldi eigenvalue solver based on the SLEPc toolkit (Hernandez *et al.* 2005). The code was tested against solutions of the Kuramoto-Sivashinsky equation (Lan & Cvitanović 2008) before being implemented for the 3D MHD equations in the shearing box, using SNOOPY as time integrator (appendix B).

2.4.3. *Cyclic dynamics in the shearing box*

An important remark is that the implementation of the shearing sheet equations in a discretized domain of finite spatial extent introduces an internal time $T_{SB} = L_y/(SL_x)$ in the system which breaks the continuous invariance of the shearing sheet equations under time translations and turns it into a discrete one. Nonlinear periodic orbits (cycles) are bound to have periods which are (*a priori* arbitrary large) integer multiples of T_{SB}. It must be emphasized that the dynamical consequences of this property of the model are under control (Herault *et al.* 2011). A qualitative dependence of the timescale of recurrent dynamics on the streamwise to shearwise aspect ratio of the solutions is nevertheless expected in all shear flows in constrained geometries (including wall-bounded ones), as this ratio sets the typical timescale of shearing of streamwise-dependent structures that ultimately extract the energy from the base flow. Note however that this observation may not carry over to spatially extended and/or stratified configurations in which recurrent forms of MRI dynamo action are also observed (Simon *et al.* 2012); see §7.2.

Appendix B.3 and C.1 explain in detail the restrictions that shear periodicity imposes on periodic orbits and how this specificity of the shearing box can actually be exploited to analyse some aspects of the dynamics in terms of discrete-time maps.

2.5. *Parameters of the study: box size, Pm and numerical resolution*

We explore the MRI dynamo transition in an elongated box with $L_x = 0.7, L_y = 20, L_z = 2$. This choice, together with the reduction to a symmetric subspace, is similar to that of a "minimal flow unit" in wall-bounded shear flows and is motivated by the necessity to reduce the nonlinear complexity of the problem (Herault *et al.* 2011). This setup is undoubtedly restrictive, and it is currently not understood which of the results obtained in such configurations should carry over to very different setups (see again discussion in §7.2). At the current stage of understanding, this approach nevertheless remains one of the most efficient to uncover some of the fundamental building blocks of the transition.

We also restrict the analysis to the dependence of the transition on the magnetic Reynolds number Rm which, as equation (2.4) indicates, is the primary bifurcation parameter in the problem. A multidimensional parametric study with respect to Re or to the box dimensions is unfortunately currently prohibitive in terms of both human and computing time. MRI dynamo action has not been found in numerical simulations in periodic, unstratified shearing boxes at $Pm < 1$ so far (Fromang *et al.* 2007). The only option currently available to address this problem is to study the detailed transition mechanisms in the $Pm > 1$ regime in which the dynamo can easily be excited, hoping that the results will provide new research directions to understand what is happening at low Pm. We set $Re = 70$ as in the work of Herault *et al.* (2011) and focus on the transition in the typical range $2 < Pm < 10$. Possible ways to address the low Pm problem will be discussed at the end of the paper in the light of the results.

The results of the paper are the outcome of several hundred thousand DNS. Such an analysis could only be performed at a moderate resolution $(N_x, N_y, N_z) = (24, 12, 36)$ (on top of which a 2/3 dealiasing rule was enforced) similar to that used in recent studies of nonlinear cycles in hydrodynamic plane Couette flow (Viswanath 2007; van Veen & Kawahara 2011). The differences between the results at this resolution and at double resolution are very minor (Herault *et al.* 2011) and do not affect any of the conclusions on MRI dynamo cycles and their bifurcations. Analysing the shape and convergence of energy spectra, we also found this resolution to be largely acceptable in our box for most DNS simulations at Re and Rm lower than 500. MRI dynamo cycles are essentially large-scale coherent structures and can therefore actually be safely followed at even higher Re and Rm using this resolution. The box size, Re, and numerical resolution remain the same throughout the paper and will not be repeated in the figure captions.

3. DNS cartography of the MRI dynamo transition

The objective of this section is to offer a phenomenological geometric and statistical perspective on the nature of the MRI dynamo transition and to uncover its possible connections with nonlinear invariant solutions.

3.1. *Cartography procedure*

The approach is inspired by earlier work on hydrodynamic shear flows (Schmiegel 1997; Moehlis *et al.* 2004*a*,*b*; Skufca *et al.* 2006; Schneider *et al.* 2007*a*) and consists in mapping the laminar-preturbulent MRI dynamo boundary in the phase space of the corresponding dynamical system (see appendix B.3), as a function of the system parameters. The high-dimensionality of this system (almost 10 000 independent degrees of freedom) makes

it impossible to probe this border in the full phase space, as a function of all system parameters. The cartography is restricted to a two-dimensional plane, with Rm in the first dimension and the amplitude of a given spatial form of initial conditions in the second dimension. The initial conditions are generated as follows. For each field component, we generate a random set of Fourier modes (white noise in spectral space), symmetrize the resulting fields to enforce reality and incompressibility, and normalize the total physical energy density to obtain a particular "noise realization". A given zero net-flux initial condition is obtained by multiplying a given noise realization by an amplitude factor A. We then perform a series of DNS for each Rm and initial condition amplitude A defined on a two-dimensional parameter grid, and the typical dynamical lifetime measured in each simulation is used to construct a two-dimensional "transition map". The lifetime definition is based on a somewhat arbitrary small threshold for the total magnetic energy below which the system is considered to have returned to the laminar state (10^{-4} in the units used – a typical dynamical state has $O(1)$ energy density). The general aspect of the maps and their qualitative interpretation do not depend critically on this definition and the threshold value used. Simulations in which the dynamics lasts for times longer than the maximum time indicated in each plot are coded with the same (dark/red) colour. The results presented below required approximately 10 0000 DNS at resolution $(N_x, N_y, N_z) = (24, 12, 36)$, each of them lasting between 500 and 700 S^{-1}.

3.2. *A fractal stability border?*

Figure 3 displays a transition map for the full problem (no imposed symmetries), and a map resolution $\delta Rm = 1, \delta A = 0.023$. Figure 4 presents another example with the dynamics restricted to the $\mathcal{A}_1$ subspace. Both maps in figures 3 and 4 display a wide, low-Rm region where return to the laminar state is quick (of the order of a few tens of shearing times) and another region in which much longer-lived three-dimensional dynamics is present. In this region, the dynamics is highly sensitive on initial conditions, i.e. a very small change in A leads to very significant changes in the history and lifetime of the dynamics. These two regions are separated by a border with an intricate geometry. Closer inspection reveals that the structure of the map, and therefore the set of initial conditions leading to long-lived transient chaos, is probably fractal. Figure 4 shows a high-resolution map (right) computed for a restricted parameter range of the map on the left. Apparently random variations of turbulence lifetime and the same colour patterns clearly replicate on smaller scales. We note that the reduction of the dynamics to a symmetric subspace does not affect the results at a qualitative level. This is good news, because operating with symmetries makes the task of understanding the transition much easier.

In the previous examples, a single noise realization was used to obtain a map of the laminar-turbulent transition border (the noise realization in the symmetry-reduced case was different from that in the full problem). Hence, these maps only explored the laminar-turbulent border along a one-dimensional line in state space. The direction of shooting was chosen randomly but once and for all before the simulations. However, there is no guarantee that results obtained this way are representative of the transition border as a whole. To test this, we computed 28 different lower resolution maps ($\delta Rm = 10, \delta A = 0.115$), each of them based on a different noise realization (figure 5). The results are interesting in two respects. First, the fractal-like structure seems to be statistically homogeneous in phase space. Except for a set of initial directions of very small measure (possibly zero), it is quite clear that shooting in any random direction will generate maps with a similar aspect. Second, the critical Rm for the onset of transient chaotic dynamics depends both on the amplitude of the initial perturbation and on the
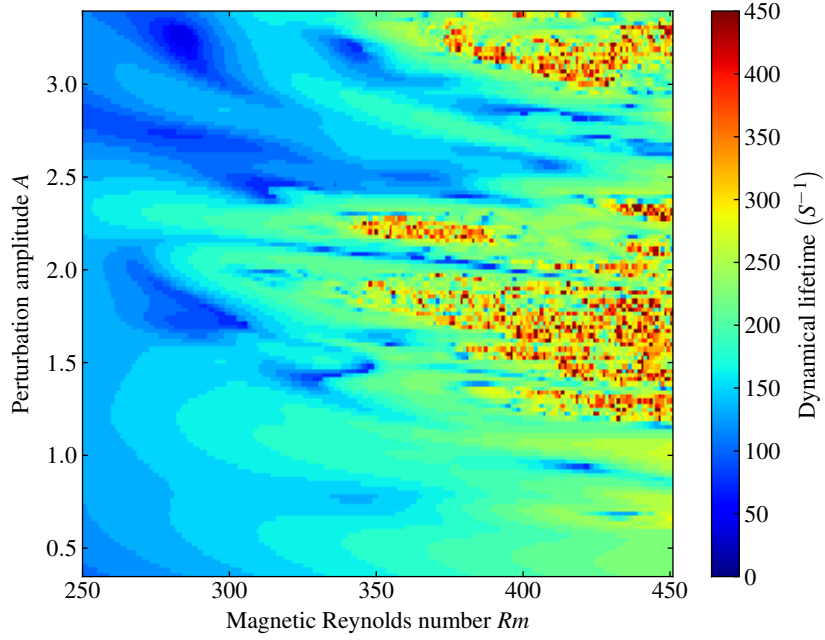
FIGURE 3. High-resolution transition map ($\delta Rm = 1, \delta A = 0.023$) as a function of initial condition amplitude A and Rm for a given noise realization and no symmetry enforced.
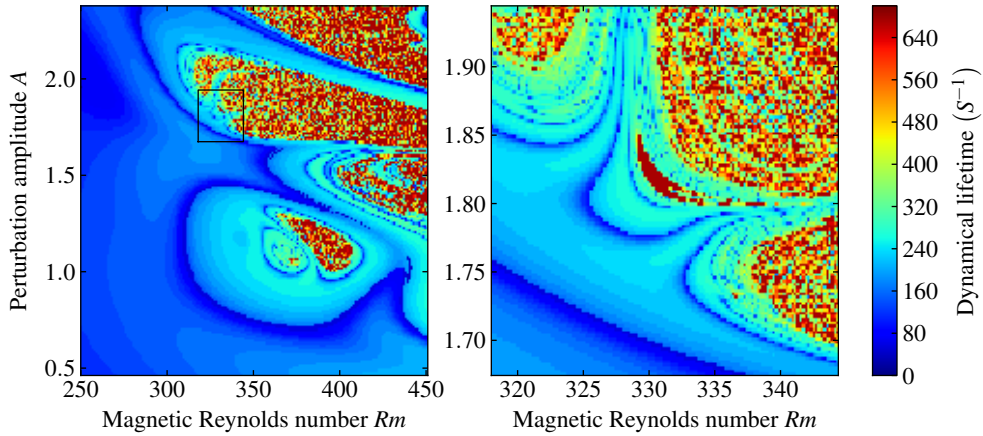

FIGURE 4. High-resolution transition maps as a function of initial condition amplitude A and Rm for a given noise realization and $\mathcal{A}_1$ symmetry enforced. Left: full map, resolution $\delta Rm = 1, \delta A = 0.0115$. Right: high-resolution map ($\delta Rm = 0.2, \delta A = 0.0023$) computed for a restricted parameter range indicated by the black rectangle in the leftmost map.

noise realization (shooting direction). For instance, it is roughly 250 in map 1 but close to 380 in map 26 (the maps are numbered from left to right and top to bottom).

The results, combined with the analysis of Rempel *et al.* (2010), strongly suggest that the MRI dynamo transition involves a chaotic saddle and that chaotic trajectories with infinite lifetime live on a zero-measure set, the so-called "edge of chaos" in transitional hydrodynamic shear flows (see references above).
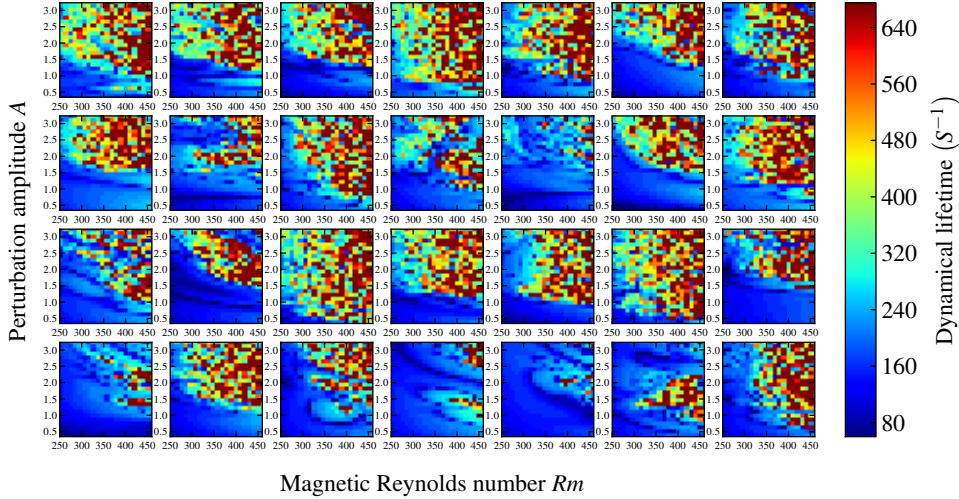
FIGURE 5. Low resolution transition maps ($\delta Rm = 10, \delta A = 0.115$) as a function of initial condition amplitude A and Rm for 28 different noise realizations.

3.3. *Islands of turbulence and transient appearance of dynamo cycles*

Much can be learned about the transition process by analysing the contents of these maps in detail. From now on, we restrict the analysis to the symmetric case, which makes it easier to identify potentially interesting dynamical behaviour. In several maps, we observe that the first chaotic regions approached as Rm is increased take the form of "islands" or elongated "fingers". Similarly, isolated zones in which the dynamics is fast-decaying penetrate into chaotic regions. Such regions are also clearly visible in similar studies of the hydrodynamic problem (Moehlis *et al.* 2004*b*).

Most simulations in these island and finger regions are characterized by a fairly extended period of recurrent dynamics with a fundamental periodicity comparable to $T_o = 2L_y/(SL_x)$ (see remarks in §2.4.3), followed by a decay to the laminar state. This observation can be made more quantitative by computing the time Fourier transform of the toroidal axisymmetric field $\overline{B}_{0y}(t)$, defined in equation (2.5) for each DNS in the map shown in figure 4, and by subsequently plotting the energy ratio between the energy integrated over the peak at the fundamental frequency $f_o = 1/T_o$ and the total energy (figure 6). Almost half of the large-scale magnetic field energy is at the fundamental frequency on average in these regions. Some areas even contain full sets of simulations that ultimately converge to truly periodic solutions. For instance, figure 6 (right) displays a zoom of the "central" structure of figure 4 (located around $A = 1.82$ and $Rm = 330$). This zoomed area contains a thin croissant-shaped region in which all simulations converge to a periodic orbit of period T_o similar to the MRI dynamo cycle reported by Herault *et al.* (2011), albeit more energetic. Other simulations in the same map converge to longer period cycles (period-4, 6, 7, 8) or to recurrent but seemingly aperiodic orbits. These long-period cycles correspond to modulated T_o oscillations with a modulation period larger than T_o. We will come back to this result in §5.4.

3.4. *Other regimes and initial conditions*

As cautioned in §2.5, it is as yet not possible to conclude that the results described so far are representative of the dynamics in all possible regimes. We checked that they were
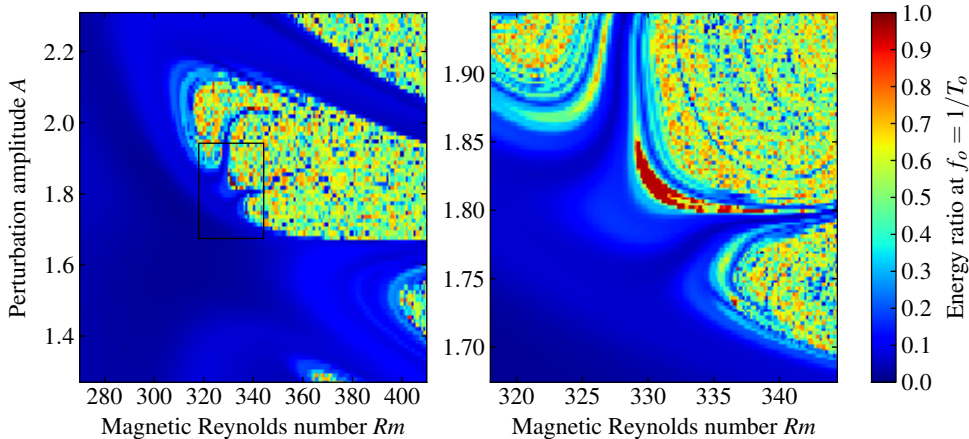
FIGURE 6. Normalized energy ratio of $\overline{B}_{0y}(t)$ at the fundamental frequency $f_o = 1/T_o$ as a function of the perturbation amplitude A and Rm for submaps of figure 4. The red/black spots indicate initial conditions lying in the basin of attraction of a stable MRI dynamo cycle.

structurally stable with respect to Re for $Re \sim 100$ ($Pm \sim 2-5$). Small increases in Re only seem to smooth out the fractal-like features and to gently reduce the coherence between cycles and turbulent dynamics. Preliminary results indicate that the situation becomes much more complex and computationally expensive to analyse as Pm tends to unity. A parametric study of transition maps with respect to the aspect ratio would also be useful, but any meaningful computational effort to span a representative range of box sizes with sufficiently small increments so as to track down interesting features is currently prohibitive. The results of Rempel *et al.* (2010) for much smaller L_y/L_x suggest that the phenomenology described above pertains to different geometric configurations.

Finally, we point out that recurrent dynamics can be excited using either zero net-flux random white noise seeds or various combinations of large-scale axisymmetric and non-axisymmetric perturbations (Herault *et al.* 2011). All simulations are ultimately energetically dominated by the large-scale sinusoidal field of equation (2.5), which is a key ingredient of the self-sustaining dynamo process.

4. MRI dynamo cycles, saddle nodes and period-doublings

Do MRI dynamo cycles play an active role in the transition process? Quantitative progress on this question first requires accurate computations of the defining features of such invariant solutions: how they are born, what their local stability properties are, etc. We now present such an analysis for two seemingly important pairs of cycles (labelled SN_1 and SN_2) spotted in the simulations presented in §3.

4.1. *Restrictions of the study and numerical convergence*

The analysis is again restricted to the Rm dependence of the problem and to the dynamics in the $\mathcal{A}_1$ symmetric subspace (both for the cycles and their eigenmodes). This facilitates the analysis and the convergence of the Newton algorithm but does not impede the essential basic mechanisms that we wish to investigate. It simply reduces the number of active simple nonlinear invariant solutions and eliminates relative periodic orbits, whose nature is fundamentally not different from that of periodic orbits.

The results were obtained with the Newton-Krylov PEANUTS solver. All of them are

converged with a relative error $||\boldsymbol{X}(T) - \boldsymbol{X}(0)||_2/||\boldsymbol{X}(0)||_2$ on the state vector smaller than 10^{-5} for the same spatial resolution as that of the DNS. Computing an accurate nonlinear MRI dynamo cycle with the solver for a given set of parameters requires ~ 10 Newton iterations, each of them involving ~ 10 Krylov iterations. Hence, a single cycle computation typically requires 100 DNS. The results presented below are the aggregation of several thousand such computations. In the few cases where continuation appeared difficult, solutions were re-calculated with double resolution, leading to only very minor differences. In almost all "hard" cases, the difficulty to converge to a cyclic solution was due to the presence of a local bifurcation in the Rm-neighbourhood of that cycle.

4.2. Saddle node 1 (SN_1)

We start by analysing the nonlinear MRI dynamo cycle found by Herault *et al.* (2011). We continued a low-resolution version of this solution obtained at $Rm = 352$ at both lower and higher Rm. The continuation curve in figure 7 (left) shows the maximal amplitude of $\overline{B}_{0y}$ over a cycle period T_o as a function of Rm in thick/dark blue line ($\overline{B}_{0y}$ is representative of the amplitude of the nonlinear solution). There are actually two cycles born out of a saddle node bifurcation at $Rm = 327.4$: a lower branch LB_1 (the solution found by Herault *et al.* (2011)), and an upper branch UB_1. UB_1 is the cycle identified in figure 6 in the croissant region. Whatever quantity is used to construct the continuation curve (maximum of $\overline{B}_{0y}$, of nonlinear stresses, etc.), UB_1 is always observed to be more vigorous than LB_1. The saddle node nature of the bifurcation is confirmed by looking at the Rm-dependence of the largest Floquet multipliers of LB_1 and UB_1 (omitting neutral multipliers corresponding to simple translations in y and z), shown in the two plots on the right of figure 7. At the bifurcation point where the solutions merge, both have a neutral eigenvalue. Slightly beyond the bifurcation point, UB_1 is actually stable, explaining the convergence of simulations in the croissant region. LB_1 has a single unstable eigenvalue near the bifurcation and is unstable for all Rm. Both cycles can be continued to much larger Rm well beyond the saddle node with no difficulty. The upper branch curve has a knee around $Rm = 430$, beyond which an asymptotic regime seems to be reached.

4.2.1. Detailed stability analysis of LB_1 and UB_1

The full stability analysis of LB_1 and UB_1 is summarized in table 1. LB_1 is originally unstable through its first Floquet multiplier Λ_1. Near the saddle node, Λ_2 and Λ_3 form a stable pair of complex conjugate multipliers. Increasing Rm, Λ_2 and Λ_3 collide and turn into a real stable pair of multipliers. Just after this collision, at $Rm = 371.24$, Λ_2 becomes larger than one. This pitchfork bifurcation results in two new branches of periodic solutions with period T_o, whose most notable feature is to be asymmetric in time at larger Rm. For these two branches, the maximum field amplitude in the first $T_o/2$ is different from that during the second half of the cycle. Closer inspection reveals that the two branches are physically identical and symmetric under a simultaneous space and time transformation which, as far as the large-scale components of the magnetic field is concerned, corresponds to a half-period phase shift combined with a change in the field polarity†. We will henceforth only focus on one of these branches, called LB_1A_1.

The stability domain of UB_1 is limited. Increasing Rm from the saddle node, the first real stable Floquet multiplier Λ_1 decreases. Originally Λ_2 and Λ_3 are stable and complex conjugate. As Rm increases, they turn into two stable real multipliers, the largest of which is responsible for a supercritical pitchfork bifurcation at $Rm = 336.54$ (dashed/red line

† This is a well-known effect in highly symmetrical dynamical systems (Swift & Wiesenfeld 1984), reported for instance in double-diffusive convection (Knobloch & Weiss 1981; Moore *et al.* 1983; Knobloch & Moore 1986) and in simple shear flow models (Moehlis *et al.* 2004*b*).
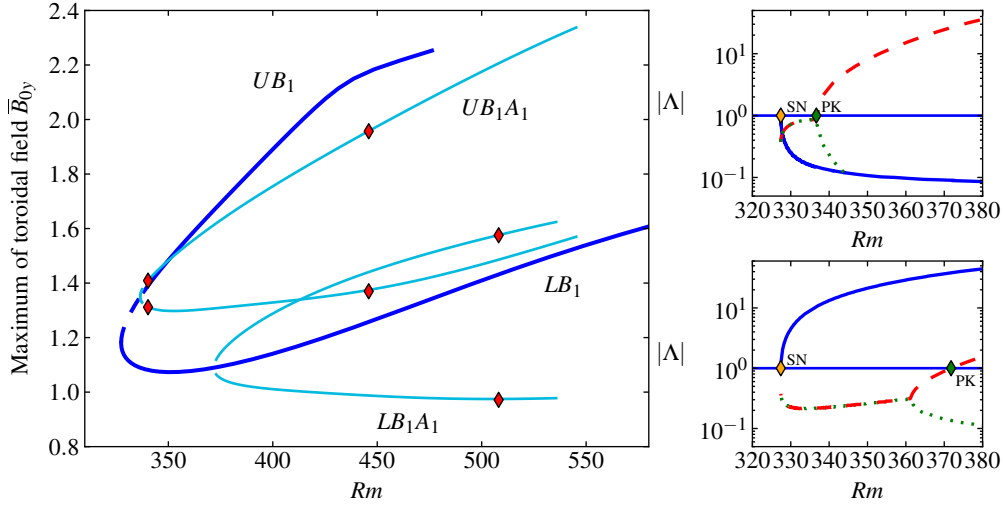
FIGURE 7. Bifurcation diagram of the SN_1 pair of cycles. Left: maximum amplitude of $\overline{B}_{0y}$ over a period cycle T_o as a function of Rm. Solid and dashed lines correspond respectively to unstable and stable solutions. Lower branch (LB_1), upper branch (UB_1) are represented using thick/dark blue lines and their asymmetric bifurcations (LB_1A_1 and UB_1A_1) are represented with thin/light-blue lines. The locations of the first period-doubling bifurcations of asymmetric cycle branches are indicated by red diamonds. Right (upper branch on top, lower branch at the bottom): norm of the first three largest Floquet multipliers as a function of Rm, with $\Lambda_1 = 1$ at the saddle node bifurcation (solid/blue line). Complex conjugate eigenvalues are superposed.

Rm	Bifurcation type	Branch	Re	Im	Re	Im	Re	Im
327.40	Saddle node		1	0	-0.30	0.23	-0.30	-0.23
336.55	Pitchfork	UB_1	1	0	0.75	0	0.14	0
371.24	Pitchfork	LB_1	37.9	0	1	0	0.14	0
340.28	P-doubling	UB_1A_1	-1	0	-0.66	0	0.16	0
439.03	Torus?	UB_1	45.1	0	-0.15	0.99	-0.15	-0.99
445.92	P-doubling	UB_1A_1	-935	0	-1	0	0.078	0
508.12	P-doubling	LB_1A_1	5279	0	-1	0	-0.15	0
~634	P-doubling	LB_1A_1	-2.63	0	-1	0	N/A	N/A

TABLE 1. Bifurcations and first three Floquet multipliers (excluding neutral multipliers) of the SN_1 pair of cycles LB_1 and UB_1 and their asymmetric child cycles LB_1A_1 and UB_1A_1 for increasing Rm. When possible, two significant decimal digits have been kept. Approximate zeroes are used to denote strongly stable multipliers of very small magnitude. The multipliers are simply sorted in descending order of magnitude here and do not necessarily correspond to the Λ_1, Λ_2 and Λ_3 terminology used in the text. Λ_1, Λ_2 and Λ_3 are only used to tag the first three Floquet multipliers at the saddle node bifurcation to follow them in Rm.

on figure 7 (top right)). This bifurcation creates two physically identical asymmetric in time periodic solutions of period T_o. We call one of them UB_1A_1.

4.2.2. Period-doublings of LB_1A_1 and UB_1A_1

We now describe the stability analysis of the asymmetric branches LB_1A_1 and UB_1A_1, whose maximum $\overline{B}_{0y}$ amplitudes during each half-cycle are used to represent their continuation in figure 7. LB_1A_1 (thin solid/light-blue line) is originally unstable as it inherits $\Lambda_1 > 1$ from its parent LB_1, while UB_1A_1 has a small stability domain

($336.5 < Rm \leq 340$), thin dashed/light-blue line). Increasing Rm from 371.24, LB_1A_1 undergoes two successive period-doubling bifurcations as two of its real Floquet multipliers become smaller than -1. The first period-doubling (red diamonds in figure 7) takes place at $Rm = 508.1$ and the second one at $Rm = 634$. We obtain two well-converged cycles of period $2T_o$ whose typical amplitudes remain close to that of LB_1A_1. A similar result is obtained for UB_1A_1 as two of its real Floquet multipliers cross -1 at $Rm = 340.28$ and $Rm = 445.92$. The first period-doubling is a primary loss of stability of UB_1A_1.

The results hint at a period-doubling cascade of MRI dynamo cycles. However, even though we managed to continue several period-doubled cycles in Rm, we found it much harder to obtain accurate results for their stability. We obtained a converged Floquet multiplier of -1 for one of the period-doubled solutions branching from UB_1A_1 but were unable to converge on the corresponding period-4 orbits. The confusion of the Newton solver may be due to the packing on the Rm line of successive period-doubling bifurcations in a Feigenbaum (1978) sequence, to the high instability of the cycles, to the close resemblance between them near bifurcation points, or to the dynamical complexity associated with global bifurcations taking place in parallel (see §5).

4.3. Saddle node 2 (SN_2)

We learned in §3 that several families of cycles probably take an active part in the transition, but there is no guarantee that the previous analysis of SN_1 cycles is representative of all such cycles. We therefore attempted to capture other cycles by feeding the Newton solver with well-chosen DNS snapshots hopefully close enough to periodic trajectories. Another simple cycle of period T_o at $Rm = 352$ that did not correspond to either LB_1 or UB_1 was found. Its continuation, displayed in figure 8 (left), shows that it is also born out of a saddle node bifurcation and is a lower branch saddle, which we henceforth call LB_2 (the upper branch is called UB_2). The saddle node nature of the bifurcation is confirmed by analysing the Rm-dependence of the Floquet multipliers (omitting once again the neutral multipliers) of LB_2 and UB_2, shown in the two plots on figure 8 (right). Just as in the previous case, both solutions have a neutral eigenvalue where they merge at the bifurcation point, located at $Rm = 334.52$. Unlike SN_1 though, the neutral eigenvalue at the saddle node is not the largest of all eigenvalues but the second largest. Hence UB_2 is born unstable and the saddle LB_2 is born with two unstable eigenvalues. Both cycles can be continued to much larger Rm, well beyond the saddle node, without any major difficulty (except again in the neighbourhood of local bifurcations described below). At large Rm, the maximum amplitude of $\overline{B}_{0y}$ and nonlinear stresses over a period both increase monotonically for increasing Rm.

4.3.1. Detailed stability analysis of LB_2 and UB_2

The stability analysis of LB_2 and UB_2 is summarized in table 2. They undergo the same kind of primary bifurcations as LB_1 and UB_1 but the detailed situation is slightly more difficult to analyse. Near the saddle node, both Λ_1 and Λ_2 of LB_2 are larger than one. As Rm increases, Λ_1 decreases, resulting in a subcritical reverse pitchfork bifurcation at $Rm = 335.25$ (dashed/red line in figure 8 (bottom right)). This bifurcation generates two branches of physically identical, asymmetric in time periodic orbits of period T_o. We only keep track of one of these branches which we hereafter call LB_2A_1. The maximum of $\overline{B}_{0y}$ over each half-cycle is represented by a pair of thin solid/light-blue lines in figure 8 (left). One notable difference with the SN_1 case is that instead of staying close to LB_2, the asymmetric branch LB_2A_1 turns at $Rm = 366.9$ and goes back to lower Rm before folding again at $Rm = 341.32$ to join UB_2 at $Rm = 347.52$. A computation of the stability of UB_2 at this point reveals that UB_2 undergoes a subcritical pitchfork bifurcation
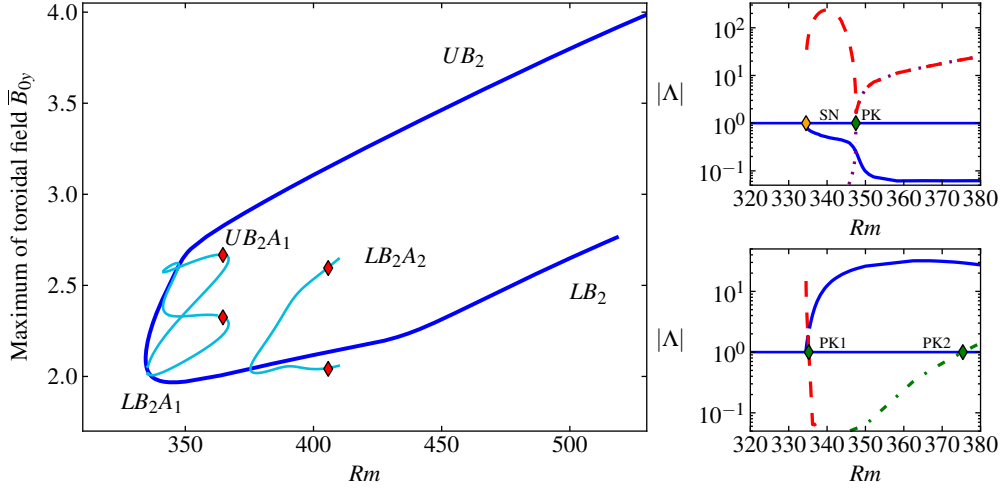
FIGURE 8. Bifurcation diagram of the SN_2 pair of cycles. Same legend as figure 7. An additional Floquet multiplier (purple dotted line) has been added in the top right plot (stability analysis of UB_2). The stability analysis of LB_2 is shown in the bottom right plot.

Rm	Bifurcation type	Branch	Re	Im	Re	Im	Re	Im
334.52	Saddle node		14.8	0	1	0	0	0.02
335.25	Rev. Pitchfork	LB_2	2.18	0	1	0	0	0.03
347.52	Pitchfork	UB_2	2.40	0	1	0	0.25	0
375.41	Pitchfork	LB_2	29.5	0	1	0	0.09	0
364.67	P-doubling	UB_2A_1	62.9	0	-1	0	-0.06	0
405.73	P-doubling	LB_2A_1	619	0	-1	0	-0.36	0

TABLE 2. Same as table 1 for the SN_2 pair of cycles LB_2 and UB_2 and their asymmetric child cycles LB_2A_1 and UB_2A_1.

associated with a fourth Floquet multiplier (purple dotted line in the top right plot of figure 8) passing through 1. Thus, LB_2A_1 is connected to both LB_2 and UB_2 (hence the second label UB_2A_1). LB_2 undergoes another pitchfork bifurcation at $Rm = 375.41$ to asymmetric in time cycles of period T_o (LB_2A_2) disconnected from UB_2.

4.3.2. Period-doublings of LB_2A_1 and UB_2A_1

The asymmetric cycles LB_2A_1/UB_2A_1 and LB_2A_2 are always unstable and undergo several period-doubling bifurcations. The first period-doubling for each branch is indicated with red diamonds in figure 8. We found it impossible in that case to converge cleanly on the period-2 solutions with the Newton solver. Just as in the previous example, this lack of convergence probably indicates that the local phase space landscape is packed with many very similar nonlinear invariant solutions.

4.4. Other periodic structures

SN_1 and SN_2 are the most frequent nonlinear MRI dynamo cycles underlying the dynamics in the symmetric subspace $\mathcal{A}_1$, but other recurrent patterns were also spotted and some transition maps indicated that preturbulent dynamics could occur at Rm as low as 250, well below the critical saddle node Rm of SN_1 and SN_2. Searching for other types of recurrences, we discovered that at least two other cycles of period T_o are involved

in transitional dynamics at $Rm < 327$. The Newton solver was able to converge to the first one. This cycle is even more energetic than UB_2 and also appears in a saddle node bifurcation. It is confined to a very small range $264 \lesssim Rm \lesssim 300$, which suggests that it takes part in the dynamics in some of the "island" regions spotted in §3. The second type of recurrence is quite different from the cycles described before, as the large-scale field component appears to reverse several times per T_{SB}. Unfortunately, we were not able to converge to the underlying nonlinear periodic orbit with reasonable accuracy.

4.5. *Relevance of period-doublings to the chaotic transition*

The results described so far indicate that supercritical period-doubling cascades (Feigenbaum 1978) of nonlinear cycles participate in the transition, but they do not actually demonstrate that such cascades are the crux of the matter. In particular, the transient nature of the dynamics suggests that it is structured around a chaotic saddle, not an attractor. It is well known that global boundary crises of preexisting attractors provide a possible route to transient chaos (see Grebogi *et al.* 1982; Kreilos & Eckhardt 2012, and discussion in §7.4), but in our simulations transient chaos is almost always found at Rm smaller than that a which even the first period-doublings occur. This suggests that other bifurcations take place in parallel to these period-doubling cascades. As we are about to show, the transition to transient chaos is most likely triggered by global homoclinic and heteroclinic bifurcations of unstable MRI dynamo cycles.

5. Chaos-generating global bifurcations of MRI dynamo cycles

Global homoclinic (respectively heteroclinic) bifurcations of nonlinear invariant solutions of a dynamical system are associated with the transverse collision in phase space between their unstable manifold W^u and their stable manifold W^s (respectively that of another invariant solution). These bifurcations are a defining signature of the dynamical stretching and folding in the vicinity of these solutions, and the Birkhoff-Smale theorem (Birkhoff 1935; Smale 1967) states that they are in fact associated with the emergence of chaotic behaviour in the system. In this section, we provide detailed numerical evidence that the unstable MRI dynamo cycles described in §4 provide the dynamical skeleton for many such bifurcations at Rm barely larger than their critical saddle node values.

The problem will be investigated in two complementary ways. At a homoclinic bifurcation, the unstable manifold of an unstable invariant solution folds back towards the solution and oscillates indefinitely around it, crossing its stable manifold an infinite number of times to form a Poincaré tangle (Ott 2002). This complex behaviour can be detected using specific techniques to visualize the geometry of the unstable manifold. The second method consists in searching for signatures of the many dynamical consequences of such bifurcations, which include the formation of Smale horseshoes, the existence of homoclinic trajectories, and that of stable cycles of arbitrarily long periods.

5.1. *Numerical procedures: Poincaré sections and low-dimensional projections*

Several dedicated numerical procedures must be used to perform this analysis. They are described step by step in appendix C. We find it useful to briefly describe two key points of the analysis here. As explained in detail in appendix C.1, the shear periodicity makes it possible to analyse the MRI dynamo flow in the shearing box as a discrete-time map (denoted by Φ_o in the following), with an iteration of the map corresponding to a time integration of the fluid equations during T_o. Looking at the state of the system strobo-scopically every T_o is equivalent to introducing a Poincaré section in the flow and makes it possible to visualize the unstable dynamics around MRI cycles more easily. Although
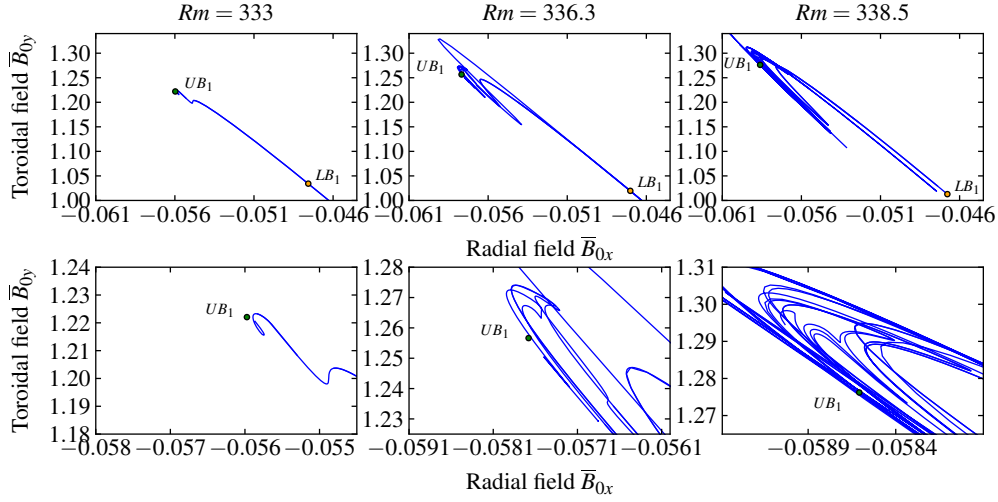
FIGURE 9. Projections of the unstable manifold of the saddle cycle LB_1 as a function of Rm for $333 < Rm < 338.5$. The plot reveals the increasingly folded geometry of $W^u(LB_1)$ resulting from the parallel formation of a homoclinic tangle of LB_1 and of a heteroclinic tangle between LB_1 and UB_1. Top: projections of $W^u(LB_1)$ in the $(\overline{B}_{0x}, \overline{B}_{0y})$ plane. Bottom: zooms on the neighbourhood of UB_1 showing the heteroclinic folding of $W^u(LB_1)$ around UB_1.

looking at full snapshots of numerical simulations every T_o is not very informative, a low-dimensional projection of the dynamics can be introduced to uncover interesting behaviour. We use a two-dimensional projection on the large-scale axisymmetric magnetic field plane $(\overline{B}_{0x}, \overline{B}_{0y})$, in which MRI dynamo cycles appear as points and their unstable manifolds as lines, if the cycles have a single unstable eigenvalue (this is always the case in the examples below). The following analysis required several 10 000 DNS at resolution $(N_x, N_y, N_z) = (24, 12, 36)$, each simulation running for several hundred shearing times.

5.2. Homoclinic and heteroclinic tangles of SN_1 cycles

5.2.1. Tangles involving LB_1

We first studied the geometry of the unstable manifold of LB_1 between $Rm = 333$ and $Rm = 338.5$. Figure 9 reveals the formation of a heteroclinic tangle between $W^u(LB_1)$ and $W^s(UB_1)$, and to a lesser extent of a homoclinic tangle of LB_1. The formation of the heteroclinic tangle is apparent in the lower zoomed plots, as $W^u(LB_1)$ starts to fold repeatedly around UB_1 as Rm increases. It is confirmed by a computation of a heteroclinic orbit between LB_1 and UB_1 (not shown). The formation of the homoclinic tangle is not obvious because $W^u(LB_1)$ first approaches UB_1 and folds around it in a very complicated way before making its first return to LB_1. Indirect evidence for this tangle was found by computing a orbit homoclinic to LB_1 whose intrinsic core length (or transition time) seems to be $3T_o$ (difficult to show rigorously in the absence of a dedicated technique; see Sterling *et al.* 1999). Figure 10 shows the time-evolution of magnetic energy along this orbit. A continuation of this orbit with respect to Rm was performed with a dedicated continuation procedure (figure 10 (right)). The bifurcation to this particular homoclinic orbit occurs at $Rm = 338.62$, smaller than the critical Rm at which the first period-doubling of either LB_1A_1 or UB_1A_1 occurs. Note that within the same tangle, homoclinic orbits with different cores are created at slightly different Rm values. Figure 10 shows that two branches of distinct homoclinic solutions exist and merge smoothly at a homoclinic bifurcation of the saddle node type.
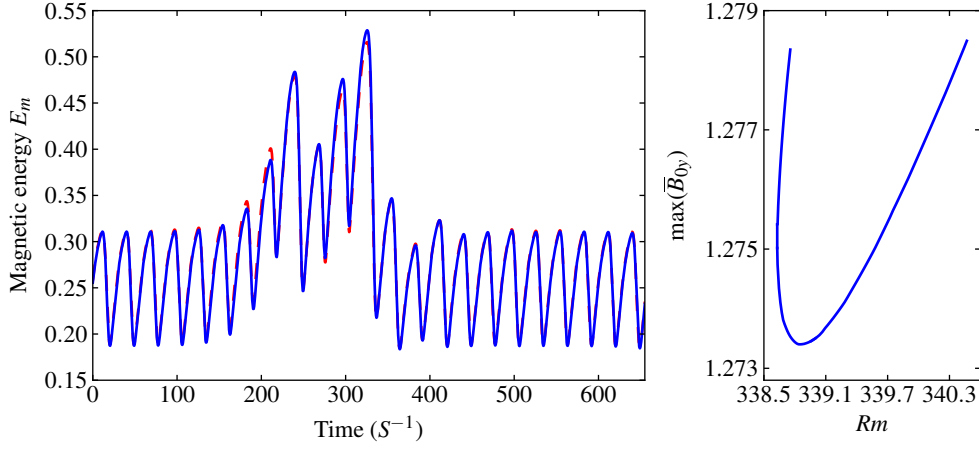
FIGURE 10. Left: time-evolution of the total magnetic energy along the least energetic homoclinic orbit of LB_1 at $Rm = 340.5$ (solid/blue line) and $Rm = 338.7$ (dashed/red line). Right: continuation curve of the homoclinic orbit representing the maximum of $\overline{B}_{0y}$ over successive snapshots taken every T_o along the homoclinic orbit, as a function of Rm.
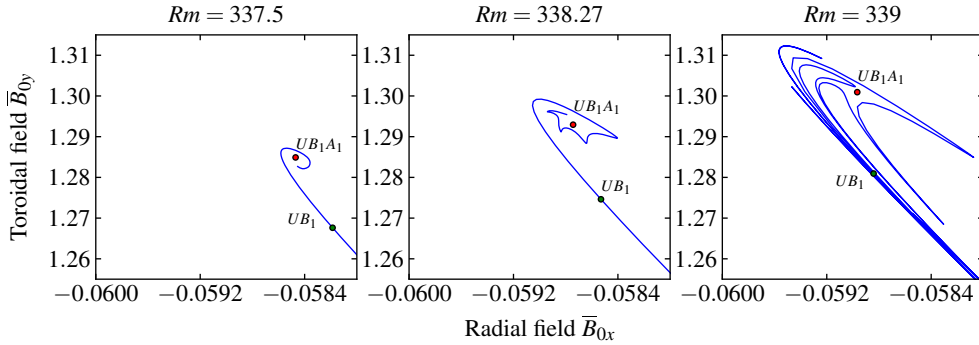

FIGURE 11. Projections of the unstable manifold of UB_1 in the $(\overline{B}_{0x}, \overline{B}_{0y})$ plane as a function of Rm for $337.5 < Rm < 339$. The homoclinic tangle is clearly visible at $Rm = 339$.

5.2.2. Homoclinic tangle of UB_1

Is this behaviour generic? We performed a similar study of the unstable manifold of UB_1 for $337.5 < Rm < 339$. Figure 11 shows a projection of $W^u(UB_1)$ at three different Rm. For $Rm = 337.5$, $W^u(UB_1)$ approaches the asymmetric solution UB_1A_1 and loops around it. At this Rm, UB_1A_1 is a stable focus (one stable real eigenvalue and two stable complex conjugate ones) and $W^u(UB_1)$ clearly feels its local attraction. At slightly larger $Rm = 338.27$, UB_1A_1 is less focusing and $W^u(UB_1)$ somehow "escapes" from its local neighbourhood. We observe the formation of spikes which tend to be attracted back to the neighbourhood of UB_1. At $Rm = 339$, the spikes have clearly been stretched along the unstable direction of UB_1 and a homoclinic tangle is born: $W^u(UB_1)$ oscillates indefinitely in front of UB_1 at ever smaller distances of UB_1 in the direction perpendicular to its unstable eigendirection, hinting at an infinite number of transverse intersections between its stable and unstable manifolds. The conclusion is supported by the computation a homoclinic orbit of UB_1 (figure 12). The continuation of this orbit with respect to Rm (figure 12 (right)) shows that two branches of distinct homoclinic solutions appear at $Rm = 338.72$ in a homoclinic saddle node bifurcation.
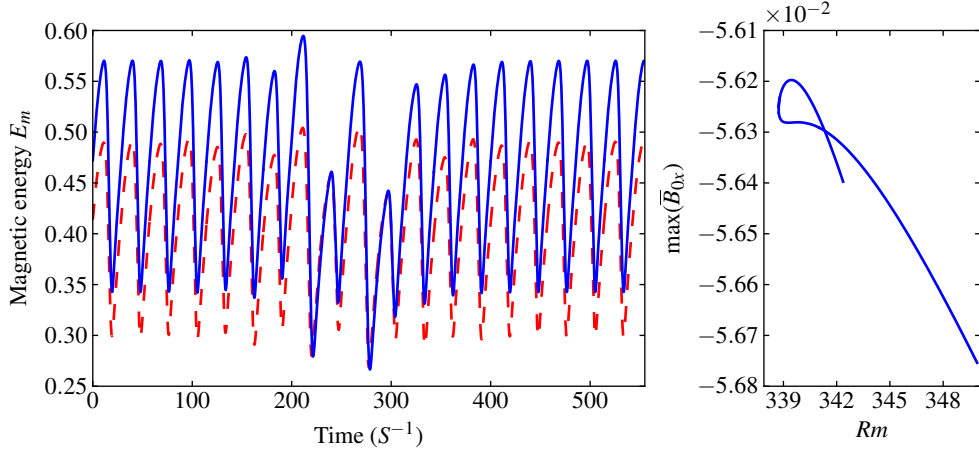
FIGURE 12. Left: time-evolution of the total magnetic energy along the least energetic homoclinic orbit of UB_1 at $Rm = 349.9$ (solid/blue line) and $Rm = 338.7$ (dashed/red line). Right: continuation curve of the homoclinic orbit representing the maximum of $\overline{B}_{0x}$ over successive snapshots taken every T_o along the homoclinic orbit, as a function of Rm.
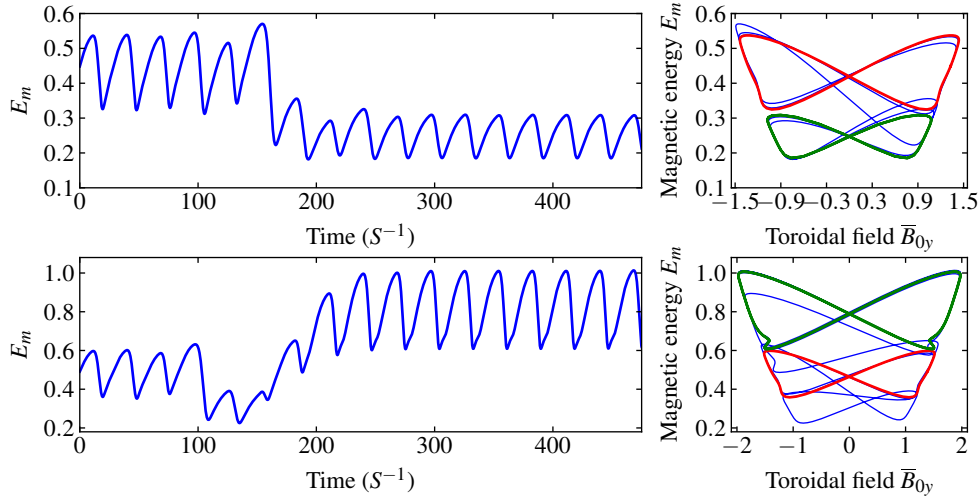

FIGURE 13. Heteroclinic orbits leaving UB_1. Top: heteroclinic orbit from UB_1 to LB_1 ($Rm = 345$). Bottom: heteroclinic orbit from UB_1 to LB_2 ($Rm = 352$). Left: evolution of magnetic energy over 500 S^{-1}. Right: phase portraits representing magnetic energy as a function of $\overline{B}_{0y}$. In both cases, the thin solid/blue line represents the heteroclinic orbit, the thick solid/red line represents the MRI dynamo cycle from which the heteroclinic trajectory departs, and the thick solid/green line represents the MRI dynamo cycle to which the trajectory asymptotes.

5.3. Other heteroclinic tangles

We found evidence for two other heteroclinic tangles. At Rm larger than 343, $W^u(UB_1)$ visits the neighbourhood of LB_1, making folds in its immediate vicinity. A heteroclinic orbit from UB_1 to LB_1 for $Rm = 345$ is shown in figure 13 (top). Another notable result is the existence of heteroclinic tangles between cycles born out of different saddle node bifurcations. At $Rm > 350$, $W^u(UB_1)$ approaches LB_2 and makes folds in its vicinity. A heteroclinic orbit between UB_1 and LB_2 at $Rm = 352$ is shown in figure 13 (bottom).
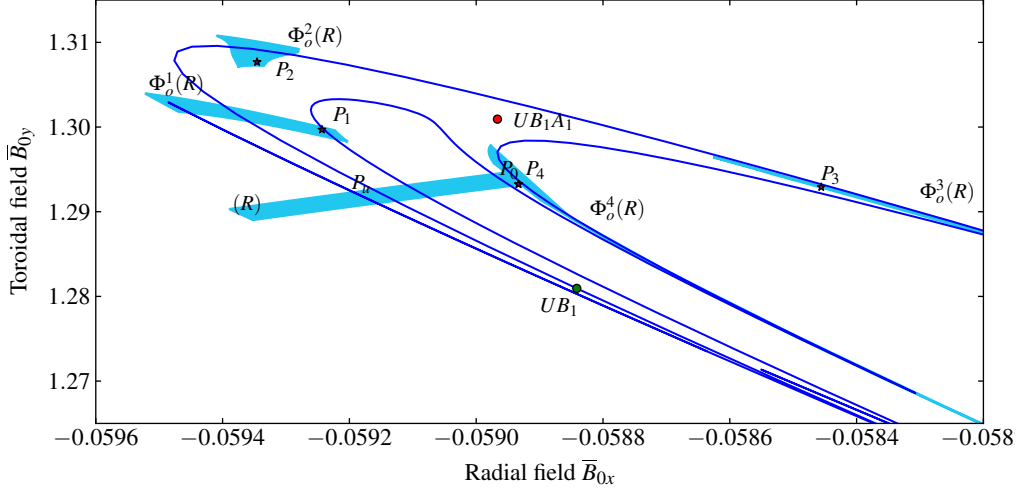
FIGURE 14. Stroboscopic dynamics in the homoclinic tangle of UB_1 projected in the $(\overline{B}_{0x}, \overline{B}_{0y})$ plane at $Rm = 339$. UB_1 and $UB_1 A_1$ are represented with filled circles. $W^u(UB_1)$ is represented by a solid/blue line. An initial patch R of phase space overlapping $W^u(UB_1)$ and its successive images under Φ_o are shown in grey/light-blue. The plot shows the intersection between R and $\Phi_o^4(R)$. The projected trajectory of the period-4 cycle is shown as a succession of stars P_0 to P_3.

5.4. *Smale horseshoe and period-doublings of stable node cycles*

We now present several supplementary numerical results which further confirm the occurrence of global bifurcations and make the connection between the tangles and the emergence of chaos in the system explicit. This paragraph is rather technical, and readers only interested in the transition phenomenology may want to jump directly to §6. The analysis is restricted to the homoclinic tangle of UB_1, but similar results can be obtained for the other identified tangles.

We first verify the occurrence of horseshoe-type dynamics (Ott 2002) predicted by the Birkhoff-Smale theorem in the tangle of UB_1. The theorem basically states that if a fixed point of a discrete-time map (such as Φ_o) has a homoclinic tangle, then a sufficiently high number of iterates of the map behaves as a horseshoe map in the neighbourhood of the fixed point. This means that if we consider a small initial subset D of state space close to UB_1 and aligned with $W^u(UB_1)$, there should exist an integer $N \geq 1$ such that the intersection between D and $\Phi_o^N(D)$ is not empty. Besides, this intersection should contain a fundamental periodic orbit of period NT_o (in the sense that it cannot be constructed from shorter-period orbits). The set of points defined as the infinite intersection $\bigcap_{k=0}^{\infty} \Phi_o^{kN}(D)$ should in fact contain a countable infinity of periodic orbits.

To confirm this behaviour in the vicinity of UB_1 at $Rm = 339$, we tried to establish the existence of long-period orbits associated with horseshoe intersections. Consider the return map representing the jth Φ_o iterate of an initial segment of $W^u(UB_1)$ versus its ith iterate, with $j > i$. The fixed points of the curves constructed that way should be periodic orbits of period $j - i$. Plotting the return maps of $\overline{B}_{0y}$ between the first iterate of Φ_o and its fifth iterate, we discovered such an approximate fixed point, which was fed into the Newton solver instructed to look for a cycle of period $4T_o$. The solver easily converged on a genuine period-4 cycle which is not a repetition of shorter cycles.

The period-4 cycle can be used to "image" the horseshoe map. The dynamical state of this cycle after each T_o can be visualized as a set of four points P_0, P_1, P_2, and P_3 in

the projection plane, shown with stars in figure 14 (P_4, the image of P_3, coincides with P_0). Let us consider the point P_u on the initial segment of $W^u(UB_1)$ closest to P_0 and construct a small patch R of phase space enclosing that point (grey/light-blue shade) by computing a set of states consisting in joint perturbations of UB_1 (whose state vector we denote by $\boldsymbol{X}_e$) along its unstable and first two stable eigenvectors $\boldsymbol{X}_u$, $\boldsymbol{X}_{s1}$, $\boldsymbol{X}_{s2}$:

$$\boldsymbol{X}(\varepsilon_u, \varepsilon_{s1}, \varepsilon_{s2}) = \boldsymbol{X}_e + \varepsilon_u \boldsymbol{X}_u + \varepsilon_{s1} \boldsymbol{X}_{s1} + \varepsilon_{s2} \boldsymbol{X}_{s2} \ . \tag{5.1}$$

The values of ε_u are taken very small compared to those of ε_{s1} and ε_{s2}, so that R is strongly elongated along the stable directions of UB_1. Each of these states is integrated by successive DNS of period T_o (Φ_o iterations) to obtain a collection of images of R under increasing powers of Φ_o (grey/light-blue shades in figure 14). The map stretches R along $W^u(UB_1)$ and contracts it in the directions perpendicular to it. After four iterations, the image $\Phi_o^4(R)$ of the original patch R intersects it in the projected plane, suggesting that Φ_o^4 is a horseshoe map. Note that P_o is both in R and $\Phi_o^4(R)$, so $\Phi_o^4(R)$ and R do indeed intersect in the full phase space. Using the return map technique with different $j - i$, we found several fundamental cycles of period 3, 4, 5, 6, 7, 8 and $9T_o$, indicating that the homoclinic tangle hosts several horseshoes, each of them corresponding to a different number of iterates of Φ_o. The evolution of magnetic energy for several such cycles, some of which were actually spotted in DNS in §3.3, is shown in figure 15. Being close to UB_1 in phase space, all the cycles display UB_1-like oscillations which appear to be modulated on the longer fundamental period of the cycles.

The previous results finally make it possible to check various mathematical predictions for two-dimensional dissipative maps relating the formation of horseshoes to that of stable long-period upper branch cycles appearing in saddle node bifurcations (Gavrilov & Shil'nikov 1972; Newhouse 1979; Robinson 1983; Palis & Takens 1993). Continuation of the long-period cycles discovered in the tangle indeed reveals that they all arise from saddle node bifurcations at slightly different Rm. The first ones to appear are a pair of period-6 cycles at $Rm = 338.72$, followed by period-5 ($Rm = 338.75$), period-7 ($Rm = 338.89$), period-4 ($Rm = 338.91$) and finally period-3 ($Rm = 339.39$). A local stability analysis shows that all upper branch solutions have a small domain of stability near the bifurcation, perhaps explaining why some of them can be spotted in DNS (§3.3), and that all of them undergo a period-doubling bifurcation at slightly larger Rm, consistent with another prediction of Yorke & Alligood (1983). Further similarities with bifurcations of the Hénon map will be briefly discussed in §7.4.

6. Chaos in the SN_1 tangles and transition maps

The objective of this short section is to offer a more intuitive illustration of the dynamical consequences of these global bifurcations and to show that they provide a natural explanation for the results of §3. We present a numerical experiment which probes the sensitivity of the system on a set of initial conditions taken along a line in phase space crossing the homoclinic tangle of UB_1 (figure 11). The idea is to mimic the experiments of §3 which shooted along random directions in phase space. We restrict the analysis to the dynamics in the vicinity of UB_1 and to a single $Rm = 341$. The same procedure could easily be repeated for other tangles. The set of initial conditions crossing the tangle is computed along the same lines as the patch R in §5.4. Projections of this locus of initial states and of $W^u(UB_1)$ and $W^u(LB_1)$ are shown in figure 16.

Figure 16 (bottom) displays the dynamical lifetime (solid/blue line) and the amplitude of $\overline{B}_{0y}$ after $t = 7T_o$ (dashed/red line), measured in each simulation as a function of a normalized curvilinear coordinate along the initial condition line. Sensitive dependence
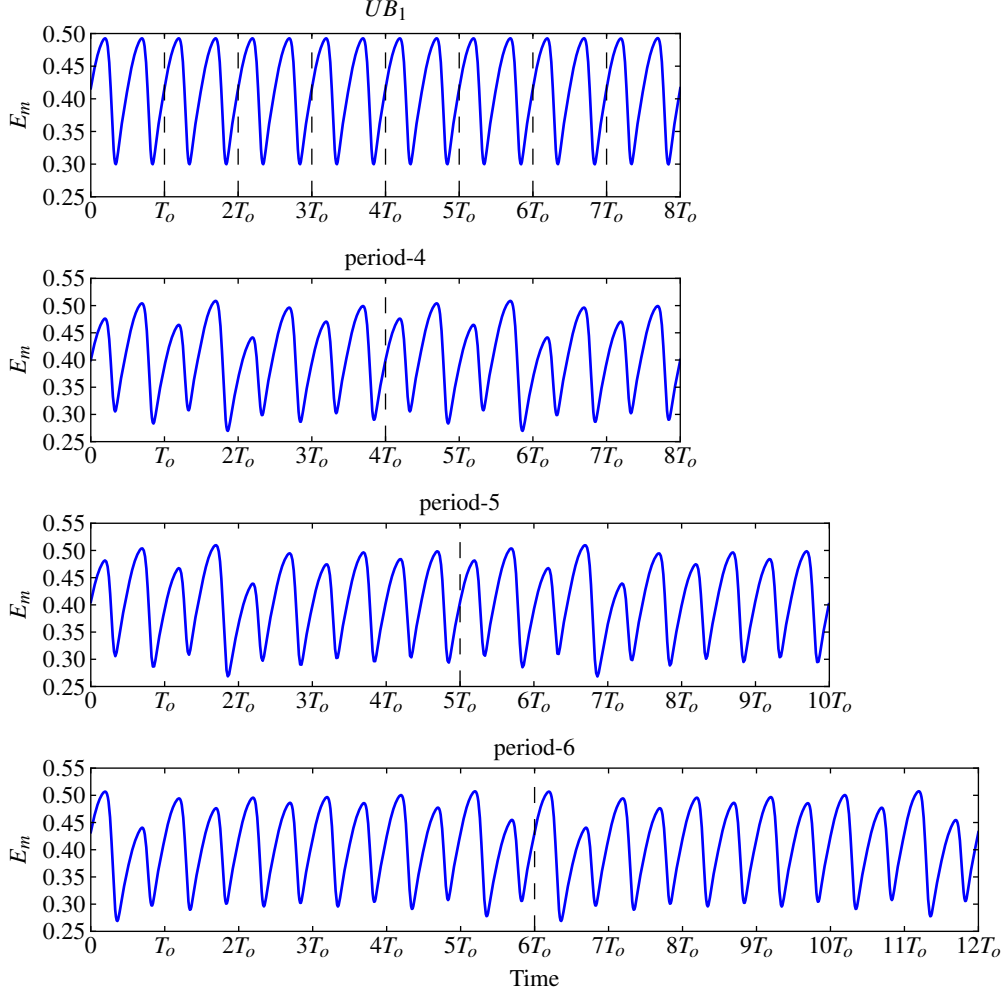
FIGURE 15. Several long-period saddle node cycles in the homoclinic tangle of UB_1. The time-evolution of UB_1 is also shown and repeated for $8T_o$ for comparison.

on initial conditions is observed as soon as the dynamics is initialized close enough to UB_1, producing a typical pattern of lifetimes reminiscent of those obtained by slicing vertically the transition maps of §3. This sensitivity is lost for continuous sets of initial conditions sufficiently far away from the tangle. In that case, the flow relaminarizes much more quickly, just like in the smooth blue/dark regions separating turbulent islands and fingers in the maps. The natural explanation for this chaotic behaviour is the stretching and folding of the dynamics in the phase space neighbourhood of UB_1.

7. Discussion

7.1. *Summary of the main results*

In this paper, we identified possible transition mechanisms to chaotic, "preturbulent" dynamics in the three-dimensional, incompressible nonlinear MRI dynamo problem in Keplerian shear flow, using the numerical shearing box framework. We focused on bifur-
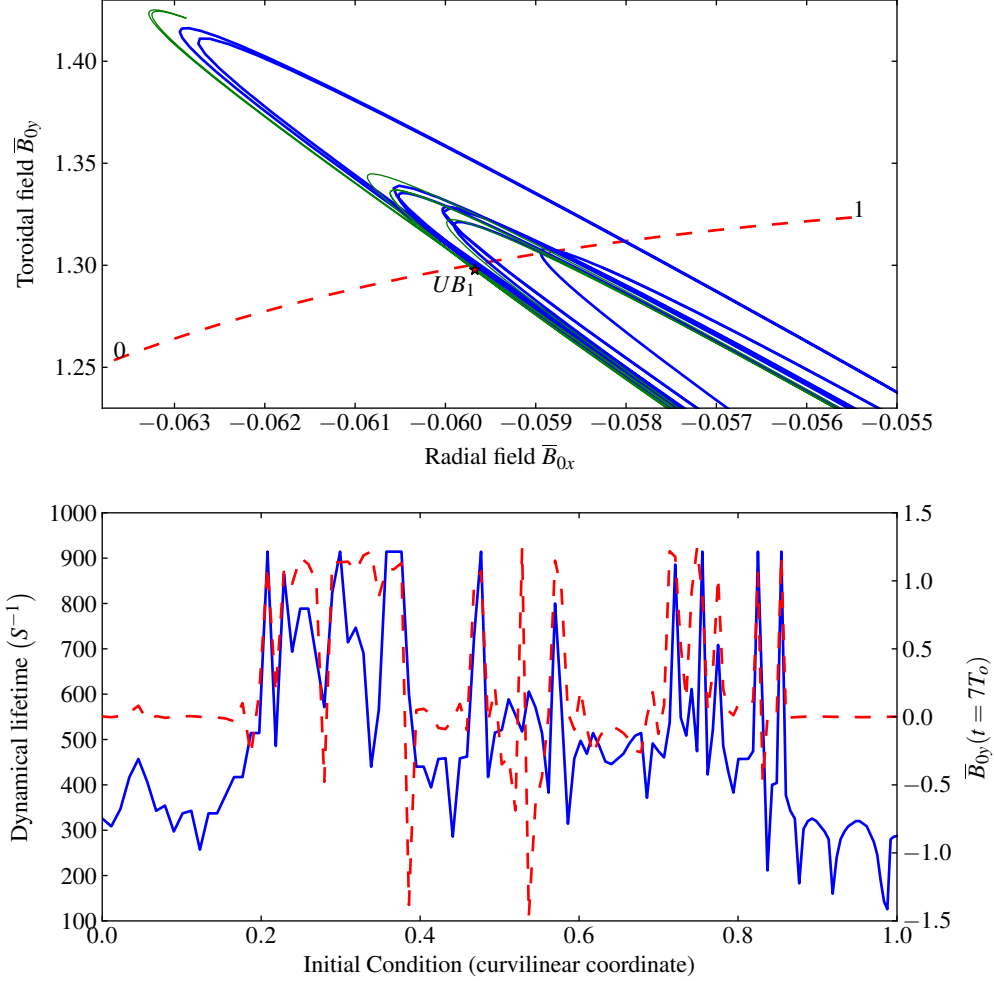
FIGURE 16. Dynamics in the vicinity of UB_1 at $Rm = 341$ as probed along a line of initial conditions across the homoclinic tangle of UB_1. Top: $(\overline{B}_{0x}, \overline{B}_{0y})$ plane projection of $W^u(UB_1)$ (thin solid/green line), $W^u(LB_1)$ (thick solid/blue line) and of the phase space line along which initial conditions are calculated (dashed/red line). Bottom: dynamical lifetime (solid/blue line) and amplitude of $\overline{B}_{0y}$ after $t = 7T_o$ (dashed/red line) for each simulation, as a function of the corresponding initial condition labelled by a normalized curvilinear coordinate along the line.

cations occurring as the magnetic Reynolds number Rm of the system is varied, for fixed "minimal" box size $(L_x, L_y, L_z) = (0.7, 20, 2)$, fixed kinetic Reynolds number $Re = 70$ and for a range of magnetic Prandtl number $2 \lesssim Pm \lesssim 8$. In most parts of the work, the dynamics was restricted to an invariant symmetric subspace to simplify the analysis.

In §3, we presented a phenomenological description of the MRI dynamo transition based on a numerical cartography of the laminar-chaotic boundary in the phase space of the system. It was shown that this transition does not occur at a well-defined critical Rm and that the stability border has a complex, fractal-like shape. The transitional dynamics is always transient but appears to be fairly recurrent and long-lived in islands or finger-shaped regions, hinting at the presence of nonlinear periodic solutions (cycles).

In §4, we described accurate computations, continuations and stability analyses of two

families of nonlinear MRI dynamo cycles whose dynamics were transiently spotted in §3. These cycles, including that computed by Herault *et al.* (2011), appear in pairs in saddle node bifurcations at Rm typical of the transition as a whole. All cycles appear either to be unstable straight from the saddle node bifurcation or to lose stability quickly in pitchfork bifurcations, resulting in the creation of new cycles whose main characteristic is to be asymmetric in time. These cycles themselves undergo period-doubling bifurcations. In some cases, period-doublings of the period-doubled cycles were also found, indicating a possible route to chaos via a cascade of supercritical period-doublings. However, it was pointed out that the first period-doublings take place at Rm larger than those at which transient chaos was typically found in §3.

This problem was addressed in §5. Studying the geometry of the unstable manifolds of several cycles studied in §4, we found that chaos-generating global homoclinic and heteroclinic bifurcations occur in the system at Rm barely larger than that of the saddle node bifurcations themselves. Quantitative verifications of several expected dynamical consequences of homoclinic bifurcations (horseshoe-type dynamics, existence of homoclinic and heteroclinic orbits and of many long-period cycles) were provided to support this claim. In §6, the sensitivity of the dynamics on initial conditions was confirmed in the vicinity of one of the cycles after a homoclinic bifurcation, and significant similarities with the transition maps described in §3 were pointed out.

Based on these results, we argue that the first germs of chaotic MRI dynamo action in this system are provided by global bifurcations of a few energy-injecting nonlinear MRI dynamo cycles whose dynamics takes place at scales comparable to the system scale at mild Rm and Re. The complex-shaped chaotic regions observed in transition maps are interpreted as signatures of the homoclinic and heteroclinic tangles surrounding these cycles in phase space. Heteroclinic connections between lower and upper branch cycles born out of different saddle nodes indicate that the system can easily jump from low energy states to higher energy states (and conversely). An increasing number of cycles involving smaller spatial scales are expected to appear in successive saddle node bifurcations at increasingly large Re and Rm and to complexify the dynamics even further.

7.2. *Connections with astrophysical accretion flows*

The highly idealized nature of the numerical experiments presented in this work (constrained geometry, incompressible flow, fairly low Re) does not make it possible to extrapolate the results directly to astrophysical accretion disks, but it is worth discussing which conclusions are likely to be at least qualitatively relevant or useful for understanding MHD turbulence and dynamo action in disks. An important first remark is that the results are the direct outcome of simulations of the full three-dimensional incompressible dissipative MHD equations, not of a mean-field model or of a very low-dimensional toy dynamical system. Besides, Herault *et al.* (2011) showed that the MRI dynamo cycles studied in both papers rely on several physical mechanisms which are all highly relevant to disks (and experiments): the Ω effect, the non-axisymmetric magnetorotational instability (which should take the form of a sheared spiral pattern in a cylindrical flow), nonlinear advection and induction mechanisms, and wave scattering processes. Several studies (Lesur & Ogilvie 2008*b*; Rempel *et al.* 2010) also suggest that chaotic saddles and periodic dynamics carry over to different geometric configurations in the incompressible framework. These arguments strongly suggest that the self-sustaining MRI dynamo process is a robut physical nonlinear phenomenon which should be present in a variety of Keplerian-like shear flows of conducting fluids (except perhaps at low Pm; see below).

Many simulations in vertically stratified Keplerian shearing boxes (Brandenburg *et al.* 1995; Stone *et al.* 1996; Gressel 2010; Davis *et al.* 2010), some of them of large horizontal

extent (Simon *et al.* 2012), also exhibit recurrent dynamics. However, several aspects of this dynamics appear to be more difficult to describe than the periodic solutions identified in this paper. In particular, magnetic reversals reported in these simulations probably result from the combined nonlinear action of many successive MRI-unstable shearing wave packets, while the cycles studied in §4 require just one simple MRI-unstable shearing wave per large-scale field reversal (Herault *et al.* 2011). The latter cycles therefore illustrate the closure of the toroidal to poloidal part of the MRI dynamo loop in its purest form and are in that sense the most simple MRI dynamo cycles that can be constructed from the physics. Much remains to be understood to connect these simple nonlinear solutions and their bifurcations to the more statistical phenomena observed in other configurations. Finally, we have not discussed in this paper the effects of vertical stratification and vertical boundary conditions, which add yet another layer of complexity to the problem. Both are notably likely to have an important impact on the typical timescale and *Pm*-dependence of the dynamo through the combined effects of magnetic buoyancy, vertical symmetry breaking and magnetic helicity expulsion (Davis *et al.* 2010; Käpylä & Korpi 2011; Simon *et al.* 2011; Oishi & Mac Low 2011).

The main conclusion of this discussion is that the incompressible shearing box model does not include all the possible effects relevant to accretion disks physics but incorporates enough ingredients of the full problem for the MRI dynamo to be active at $Pm > 1$ in its simplest possible form. The results therefore seem to provide a tangible starting point to address the question of the existence of an MRI dynamo mechanism at low Pm from a quantitative nonlinear dynamics perspective. In particular, they make it possible to ask computationally challenging but well-defined questions such as whether a self-sustaining MRI dynamo process, MRI dynamo cycles (not necessarily those described in this paper) and chaos-generating bifurcations are present in this regime. Multi-parameter explorations along the lines of the numerical study presented in §3 represent a complementary avenue of research in this respect.

The results may to a lesser extent also be useful for studying how (MHD) turbulent angular momentum transport varies with the various dimensionless parameters of the problem. All the cycles found in the range of magnetic Prandtl numbers investigated transport a significant amount of angular momentum, comparable to or larger than the typical transport rates estimated in most past DNS studies of the problem†. However, whether a few large-scale cycles, most notably the more energetic upper branch solutions, are representative of fully turbulent states remains to be assessed. Making a representative census of all the organizing cycles present at a given Rm and Re is probably required to obtain reliable estimates of the magnitude of turbulent transport using periodic orbit theory (Cvitanović 1992) but appears difficult in such a high-dimensional system in turbulent regimes. A similar problem is currently investigated in hydrodynamic turbulence (Cvitanović & Gibson 2010; Chandler & Kerswell 2013).

7.3. *Connections with dynamo theory and experiments*

The results also confirm the subcritical, non-kinematic nature of the MRI dynamo. In particular, MRI dynamo cycles do not bifurcate linearly from a preexisting turbulent hydrodynamic state. The electromotive force involved in the self-sustaining regeneration process of the large-scale axisymmetric field is also always observed to be a complicated nonlinear time-delayed function of the field in the configuration studied, indicating that the coherent, large-scale periodic dynamics described by Herault *et al.* (2011) cannot

---

† Quite remarkably, in the configuration studied, the Maxwell stress throughout the periodic dynamics is dominated by the correlation between the large-scale axisymmetric "dynamo" field components $\overline{B}_{0x}$ and $\overline{B}_{0y}$, not by the self-correlations of non-axisymmetric MRI disturbances.

be simply described in terms of classical mean-field theory. It may be possible to fit numerically the $\overline{\mathcal{E}}$ versus $\overline{\boldsymbol{B}}$ relation using various methods but a rigorous, physically motivated statistical closure theory valid for generic physical configurations remains to be developed in connection with the observations made in §7.2.

A second significant result in this context is the very explicit identification of global homoclinic and heteroclinic bifurcations in a three-dimensional MHD system. Similar bifurcations have long been invoked in the context of the geodynamo and experimental dynamos (see e.g. Gallet *et al.* 2012; Gissinger 2012) and there have actually been reports of heteroclinic dynamo orbits in the VKS experiment (Monchaux *et al.* 2009). A compelling observation very likely related to the occurrence of such bifurcations is the remarkable dynamical complexity offered by the MRI dynamo and other instability-driven dynamos (Cline *et al.* 2003; Tobias *et al.* 2011) even in fairly low-resolution three-dimensional numerical experiments. Not only are fully three-dimensional, large-scale (comparable to the size of the domain) MRI dynamo cycles easy to excite, the problem also contains all the germs of chaotic dynamo action, a hallmark of many astrophysical dynamos. It is therefore tempting to conjecture that instability-driven dynamos relying on self-sustaining processes play an important role in the generation of large-scale, time-dependent magnetic fields in differentially rotating astrophysical flows such as those encountered in stellar interiors. Global simulations might be able to test this in the future.

This work may finally turn out to be useful to future laboratory experiments on dynamos and on the MRI. The low Pm issue discussed earlier is also important in this context, as all experiments to date have been conducted in liquid metals for which $Pm \ll 1$, but upcoming plasma dynamo experiments may make it possible to study the MRI dynamo in Keplerian-like flows in $Pm > 1$ regimes (Collins *et al.* 2012). Another possible caveat relative to the connection with experiments is that the shearing box has no walls and no curvature. Similar work in wall-bounded curved geometries is needed to assess the existence of MRI dynamo cycles in this kind of configuration and to make quantitative predictions for experimental MRI dynamo thresholds and periods. As explained by Herault *et al.* (2011), the essential triad couplings characteristic of all self-sustaining processes in shear flows do not require walls. The existence of time-periodic nonlinear hydrodynamic solutions in *wall-bounded* shear flows (Kawahara & Kida 2001; Viswanath 2007; Kreilos & Eckhardt 2012) also strongly suggests that the time-periodic nature of the solutions computed in this paper is not a shearing box artefact. Of course, MRI dynamo cycle periods in wall-bounded geometry should not be quantized.

7.4. *Connections with other chaotic systems and hydrodynamic transition of shear flows*

The dynamical behaviour described in the previous sections has much in common with several well-known simpler dynamical systems, such as chaotic scattering by three potential hills (Ding *et al.* 1990) and, perhaps more importantly, with the bifurcations of the two-dimensional Hénon map (Hénon 1976; Grebogi *et al.* 1983; Sterling *et al.* 1999). The sequence of global bifurcations uncovered in §5 is actually almost identical to that following the saddle node bifurcation to period-1 cycles in that map (Grebogi *et al.* 1987; Goswami & Basu 2002). We did not investigate the question but it cannot be ruled out the closure of $W^u(UB_1)$ is a Hénon-type attractor in a limited range of Rm.

The most interesting connection is with recent advances on the problem of hydrodynamic transition of shear flows, in particular with the work of Kreilos & Eckhardt (2012) on plane Couette flow. They describe a basin boundary crisis (Grebogi *et al.* 1982; Ott 2002) which results from the collision between a chaotic attractor and the stable manifold of a lower branch saddle equilibrium. Indirect evidence for a homoclinic tangle of a saddle solution has also been reported in Couette flow by van Veen & Kawahara (2011).

The results altogether suggest that various homoclinic and heteroclinic crises involving different types of repelling and attracting structures are possible in these problems. Their occurrence probably depends on the flow geometry, aspect ratio and detailed properties of the nonlinear saddle node solutions taking part in the transition process.

Note finally that further bifurcations may occur at larger Re or Rm in these problems and change the nature of the dynamics, as exemplified by the Lorenz system (Sparrow 1982). Multiple crises scenarios could perhaps be investigated with the techniques used in this paper, but the task appears difficult in view of the dynamical complexity already present at mild parameter values. Another interesting research direction in this respect is the possible route to spatiotemporal chaos in spatially extended systems proposed by Pomeau (1986) and recently explored by Manneville (2009); Willis & Kerswell (2009); Moxey & Barkley (2010); Barkley (2011); Avila *et al.* (2011).

Appendix A. DNS techniques - SNOOPY and the shearing box

A.1. *Shear periodicity*

The SNOOPY code is a pseudo-spectral code (Canuto *et al.* 1988) for the direct numerical simulation of the three-dimensional, incompressible dissipative MHD equations. It provides an implementation of the shearing box model assuming simple spatial periodicity in the y and z directions. Due to the presence of shear, the x direction cannot be taken periodic. To see this, consider the left-hand side of the Navier-Stokes and induction equations (2.1)-(2.2) in the presence of a linear shear flow $\boldsymbol{U}_S = -Sx\boldsymbol{e}_y$:

$$\frac{\partial \boldsymbol{\Psi}}{\partial t} - Sx\frac{\partial \boldsymbol{\Psi}}{\partial y} = \cdots \ , \tag{A 1}$$

where $\boldsymbol{\Psi}$ is either $\boldsymbol{u}$ or $\boldsymbol{B}$. This equation has an explicit linear x-dependence which prevents any periodic decomposition of solutions. In more physical terms, assuming that a non-axisymmetric (y-dependent) physical structure is strictly periodic in x at some time t, then it is clear that the periodicity is destroyed as the structure is sheared. In order to use a spectral representation in the simulations, the solution is to go to a sheared Lagrangian frame of reference (see Umurhan & Regev 2004) defined according to

$$x' = x \ , \quad y' = y + Sxt \ , \quad z' = z \ , \quad t' = t. \tag{A 2}$$

In that frame, equation (A 1) transforms into

$$\frac{\partial \boldsymbol{\Psi}}{\partial t'} = \cdots \ , \tag{A 3}$$

which does not have any explicit dependence on x'. Periodic boundary condition in x' can be assumed, hence the term shear periodicity.

A.2. *Spectral representation: shearing waves*

The previous discussion makes it clear that any field $\boldsymbol{\Psi}$ in the discretized sheared Lagrangian frame (x_p', y_q', z_r') can be transformed to Fourier space according to

$$\hat{\boldsymbol{\Psi}}_{l,m,n} = \sum_{-N_x/2}^{N_x/2} \sum_{-N_y/2}^{N_y/2} \sum_{-N_z/2}^{N_z/2} \boldsymbol{\Psi}(x_p', y_q', z_r') \exp\left[-i(k_{x,l}' x_p' + k_{y,m}' y_q' + k_{z,n}' z_r')\right] , \quad (A\,4)$$

where the $k_{x,l}' = 2\pi l/L_x$ are the Lagrangian Fourier wavenumbers in the periodic x' direction and the $k_{y,m}' = 2\pi m/L_y$ and $k_{z,n}' = 2\pi n/L_z$ are the Fourier wavenumbers in the periodic y' and z' directions. Using equation (A\,2) in equation (A\,4) to look at the evolution in the Eulerian frame of reference (x, y, z), the shearing of a non-axisymmetric plane wave with given wavenumber $k_{y,m}'$ in the $y' = y$ direction and Lagrangian wavenumber $k_{x,l}'$ in the x' direction is described by a time-dependent Eulerian wavevector

$$k_x(t) = k_{x,l}' + S k_{y,m}' t , \quad k_y = k_{y,m}' , \quad k_z = k_{z,n}'. \quad (A\,5)$$

This equation translates the physical observation that the typical scale of non-axisymmetric structures along the x direction becomes increasingly smaller as the structure gets sheared. Waves whose wavevectors follow this kind of evolution are called shearing waves (Lord Kelvin 1887; Orr 1907). As a result, the right hand side of equation (A\,3) (the kind of equation integrated in practice) is explicitly dependent on time, as any term involving spatial derivatives with respect to the shearwise direction (for instance the dissipative terms) now involves expressions of the form (A\,5) in spectral space.

A.3. *Remapping procedure*

Equation (A\,5) shows that the "effective" wavenumber grid used to compute spatial derivatives in spectral space is sheared. Now, if we simply consider the nonlinear evolution of a given initial set of shearing waves defined on such a grid, some physical nonlinearities and therefore some physics will be missed. Shearing waves rapidly evolve into strongly trailing $(k_x(t)k_y > 0)$ sheared structures with ever smaller scale in x and are therefore dissipated extremely efficiently (Knobloch 1985; Korycansky 1992). This kind of dynamics is not self-sustaining. Even worse, all the Fourier modes available to describe the dynamics end up strongly trailing after some time, after which there are no modes left to describe new leading waves $(k_x(t)k_y < 0)$ that could potentially be *physically excited*. This problem is solved by introducing a remapping procedure. We show in figure 17 a cartesian wavenumber grid $(k_{x,l}', k_{y,m}', k_{z,n}')$ (dashed/blue lines) coinciding with the simulation grid at $t = 0$. The simulation grid (solid/black lines) is sheared according to equation (A\,5) as time increases but coincides with the reference grid every $T_{SB} = L_y/SL_x$. Indeed, after T_{SB}, the effective wavenumber grid is

$$k_x(T_{SB}) = k_{x,l}' + k_{y,m}' S\,T_{SB} = k_{x,l+m}' , \quad k_y = k_{y,m}', \quad k_z = k_{z,n}' . \quad (A\,6)$$

In other words, a shearing wave with wavenumber $k_{y,m}'$ in the y direction and initial wavenumber $k_{x,l}'$ in the x direction can be described at $t = T_{SB}$ as a shearing wave with the same wavenumber $k_{y,m}'$ in the y direction but a different wavenumber $k_{x,l+m}'$ in the x direction. This makes it possible to reproject the fields on the reference wavenumber grid at this particular time. For instance, the Fourier coefficient $\hat{\boldsymbol{\Psi}}_{l,m,n}$ during the first T_{SB} of the simulation becomes $\hat{\boldsymbol{\Psi}}_{l+m,m,n}$ between T_{SB} and $2\,T_{SB}$, and so on. Beside this simple reallocation of Fourier space, the Fourier coefficients of trailing shearing waves whose absolute value of the radial wavenumber $|k_x|$ exceeds $\pi N_x/L_x$ (the Nyquist wavenumber) at T_{SB} are set to zero at the corresponding time. The corresponding basis vectors (red
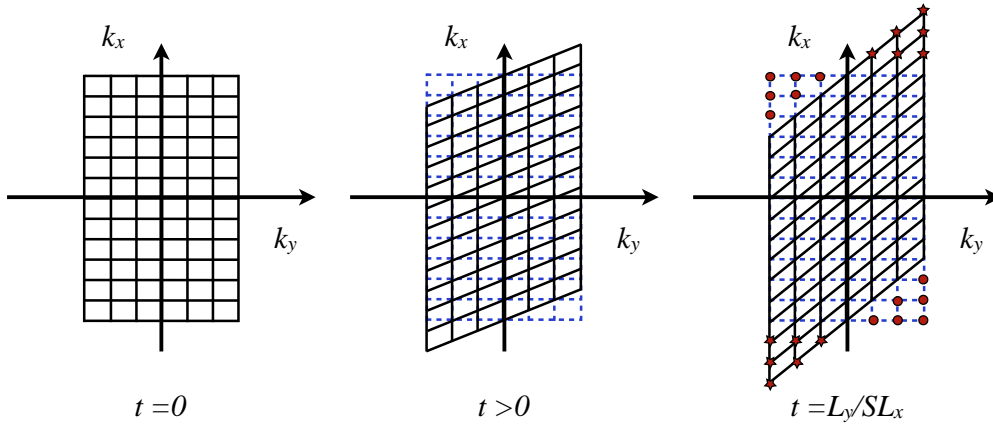
FIGURE 17. Time-evolution of the wavenumber grid. The sheared grid is shown in solid/black line, the reference cartesian grid in dashed/blue line. The two grids coincide after $t = T_{SB}$, except for the points shown with symbols. Red stars indicate strongly trailing wavevectors ($k_y k_x > 0$) with $|k_x| > \pi N_x / L_x$. The corresponding Fourier basis vectors are pruned and replaced with new leading basis vectors ($k_y k_x < 0$), shown as full/red circles on the rightmost sketch.

stars in the figure) are pruned and replaced by new shearing wave basis vectors with strongly leading wavenumber in the wavenumber grid (full/red circles).

Because we only update the basis of representation of the fields during the remapping procedure and not the fields themselves, the procedure does not affect artificially the physical evolution as long as the simulations are well-resolved. The pruned wavevectors represent strongly trailing waves which have already been heavily damped by dissipative processes when they are pruned. We always find that pruning losses are negligible in SNOOPY compared to the physical dissipation for well-resolved simulations (Lesur & Longaretti 2005). The remapping procedure does not by itself inject energy into new leading waves either, but merely provides room for them in the wavenumber grid. A pseudo-spectral method with dealiasing is used to compute all nonlinear terms of equations (2.1)-(2.3) at each time step. These terms describe the physical nonlinearities of the system and are the only ones that can seed energy into leading waves when the corresponding basis wavevectors are introduced, as the energy content of these new waves is strictly enforced to be zero when the remapping is performed (Herault *et al.* 2011).

A.4. *Symmetries*

Nagata (1986) identified several possible symmetries for three-dimensional nonlinear hydrodynamic solutions in centrifugally unstable (Rayleigh-unstable) Taylor-Couette flow in the thin-gap limit, which corresponds to a cartesian wall-bounded plane Couette flow rotating along its spanwise z axis. Several similar symmetries can be derived for MHD flows in the Keplerian shearing box. We consider a physical domain of size (L_x, L_y, L_z) and introduce a reference frame comoving with the fluid at $L_x/2$:

$$\tilde{y} = y - \frac{L_x}{2} St \ . \tag{A 7}$$

Most simulations and nonlinear solutions described in the paper are restricted to a symmetric $\mathcal{A}_1$ subspace in which the fields are described according to :

$$\boldsymbol{u}: \begin{cases} u_x &= \quad u_{x,\mathrm{ee}}(t)\cos\left(k_{z\mathrm{e}}z\right)\sin\left(k_{y\mathrm{e}}\tilde{y}+k_x(t)x\right) \\ &+ \quad u_{x,\mathrm{oo}}(t)\cos\left(k_{z\mathrm{o}}z\right)\cos\left(k_{y\mathrm{o}}\tilde{y}+k_x(t)x\right) \\ u_y &= \quad u_{y,\mathrm{ee}}(t)\cos\left(k_{z\mathrm{e}}z\right)\sin\left(k_{y\mathrm{e}}\tilde{y}+k_x(t)x\right) \\ &+ \quad u_{y,\mathrm{oo}}(t)\cos\left(k_{z\mathrm{o}}z\right)\cos\left(k_{y\mathrm{o}}\tilde{y}+k_x(t)x\right) \\ u_z &= \quad u_{z,\mathrm{ee}}(t)\sin\left(k_{z\mathrm{e}}z\right)\cos\left(k_{y\mathrm{e}}\tilde{y}+k_x(t)x\right) \\ &+ \quad u_{z,\mathrm{oo}}(t)\sin\left(k_{z\mathrm{o}}z\right)\sin\left(k_{y\mathrm{o}}\tilde{y}+k_x(t)x\right) \end{cases}, \qquad (\mathrm{A}\,8)$$

$$\boldsymbol{B}: \begin{cases} B_x &= \quad B_{x,\mathrm{eo}}(t)\cos\left(k_{z\mathrm{e}}z\right)\sin\left(k_{y\mathrm{o}}\tilde{y}+k_x(t)x\right) \\ &+ \quad B_{x,\mathrm{oe}}(t)\cos\left(k_{z\mathrm{o}}z\right)\cos\left(k_{y\mathrm{e}}\tilde{y}+k_x(t)x\right) \\ B_y &= \quad B_{y,\mathrm{eo}}(t)\cos\left(k_{z\mathrm{e}}z\right)\sin\left(k_{y\mathrm{o}}\tilde{y}+k_x(t)x\right) \\ &+ \quad B_{y,\mathrm{oe}}(t)\cos\left(k_{z\mathrm{o}}z\right)\cos\left(k_{y\mathrm{e}}\tilde{y}+k_x(t)x\right) \\ B_z &= \quad B_{z,\mathrm{eo}}(t)\sin\left(k_{z\mathrm{e}}z\right)\cos\left(k_{y\mathrm{o}}\tilde{y}+k_x(t)x\right) \\ &+ \quad B_{z,\mathrm{oe}}(t)\sin\left(k_{z\mathrm{o}}z\right)\sin\left(k_{y\mathrm{e}}\tilde{y}+k_x(t)x\right) \end{cases}, \qquad (\mathrm{A}\,9)$$

where the e and o subscripts indicate that the associated discrete wavenumbers are based on even and odd relative integers, respectively. $k_x(t)$ in each individual trigonometric expression is defined implicitly by equation (A 5) using the k_y wavenumber of the same expression. This symmetry is conserved by the MHD equations (2.1)-(2.3).

Appendix B. Newton solver - PEANUTS

The main difficulty in interfacing a Newton solver with a high-dimensional PDE integrator comes from the construction of a mapping between the full multidimensional representation of fields most often used in DNS and a reduced one-dimensional state vector representation required for the Newton solver. The problem is particularly tedious for incompressible fluid dynamics and/or when spectral dealiasing is used, as one must analyse carefully which modes of the full representation must be kept in the state vector representation in that case to avoid numerical trouble associated with singular algebra. This appendix describes how to switch from the full three-dimensional representation of MHD fields in SNOOPY to a reduced one-dimensional state vector representation in the Newton solver PEANUTS. We also discuss the important issue of enforcing spatial and temporal phase constraints in the shearing box to compute simple invariant solutions.

B.1. *Mode counting*

We wish to count the number of independent real variables of the state vector to obtain an invertible problem, starting from $N_x N_y N_z$ real values in physical space for each field component. The divergence-free constraint on both the velocity and magnetic field reduces the number of independent field components to 4. We also restrict the dynamics to a subspace in which the mean velocity is zero, which reduces the number of independent variables for each velocity component by 1. Finally, since the shearing box equations conserve magnetic flux, all box-averaged magnetic field components should vanish, reducing the number of independent variables for each magnetic component by 1. The number of independent variables for the MHD equations in the shearing box in three dimensions is therefore $N_v = 4(N_x N_y N_z - 1)$. If we also reject the Nyquist modes, we find

$$N_v = 4(N_x N_y N_z - 2) . \qquad (\mathrm{B}\,1)$$

If dealiasing is used, N_i ($i = x, y, z$) is always taken a multiple of 3 and 2, so that $n_i = 2N_i/3$ are integers. The dealiasing procedure also zeroes the Fourier components in the Nyquist planes $n_i/2$, leaving $n_i - 1$ variables in each direction and a total count of

	Hold variables	wavenumber range	Missing component
$k_z \neq 0$	$\tilde{\Psi}_x$ and $\tilde{\Psi}_y$	$k_z = 1$ to $(n_z - 2)/2$	$\tilde{\Psi}_z = -[k_x\tilde{\Psi}_x + k_x\tilde{\Psi}_y]/k_z$
$k_z = 0$ $k_y \neq 0$	$\tilde{\Psi}_z$ and $\tilde{\Psi}_x$	$k_y = 1$ to $(n_y - 2)/2$	$\tilde{\Psi}_y = -k_x\tilde{\Psi}_x/k_y$
$k_y = 0$ $k_x \neq 0$	$\tilde{\Psi}_y$ and $\tilde{\Psi}_z$	$k_x = 1$ to $(n_x - 2)/2$	$\tilde{\Psi}_x = 0$
$k_x = 0$	removed		

TABLE 3. State vector mappings. For each Fourier mode, hold variables denote variables kept during the forward mapping between the DNS and Newton codes. The missing components are those recovered in the reverse mapping from the Newton code to the DNS codes.

$(n_x - 1)(n_y - 1)(n_z - 1)$ per field component. The same number of constraints as before must be subtracted, leading to a number of independent variables equal to

$$N_v = 4\left[(n_x - 1)(n_y - 1)(n_z - 1) - 1\right] \ . \tag{B 2}$$

B.2. *Reduction of field variables*

The procedure to switch back and forth between the full three-dimensional representation of complex Fourier-transformed fields $\tilde{\boldsymbol{\Psi}}$ (with $\boldsymbol{\Psi} = \boldsymbol{u}$ or $\boldsymbol{B}$) and the reduced state vector representation of size N_v is summarized in table 3 for the dealiased problem (the only one of practical importance). In the forward mapping (DNS→Newton), only two field components are kept for each wavenumber to satisfy the incompressibility constraint, while $\boldsymbol{k} = \boldsymbol{0}$ modes are suppressed to ensure zero mean velocity and magnetic flux conservation. In the reverse mapping (Newton→DNS), the missing component is recovered thanks to the incompressibility condition expressed in Fourier space. The wavenumber range indicated in the table results from the real nature of the physical fields (the complex Fourier amplitudes for the missing wavenumbers are recovered by complex conjugation).

B.3. *Newton algorithm, phase constraints and shear periodicity*

A general method for imposing constraints in the Newton algorithm to compute relative periodic orbits of wall-bounded shear flows is described by Viswanath (2007). The shearing box case is a bit special and should be discussed in some detail. We denote a full state vector in the Newton solver representation by $\boldsymbol{X}(t)$. This vector of size N_v contains all the independent complex Fourier modes of all the independent components of the physical fields $(\boldsymbol{u}, \boldsymbol{B})$. Our dynamical system is formally described by

$$\frac{d\boldsymbol{X}}{dt} = \boldsymbol{F}(\boldsymbol{X}) \ , \tag{B 3}$$

where $\boldsymbol{F}$ is a nonlinear "MRI dynamo operator". This system can be integrated by DNS, and a Newton solver is used to compute relative periodic orbits of period T obeying

$$\boldsymbol{X}(\boldsymbol{X}_0, T) = \boldsymbol{\tau}(\boldsymbol{X}_0) \ , \tag{B 4}$$

where $\boldsymbol{X}_0$ is the state of the system at $t = 0$ and $\boldsymbol{\tau}$ is a translation operator in the y and z directions, which are the two directions of invariance of the shearing box (recall that spatial periodicity is assumed along these directions). In principle, the problem has $N_t = N_v + 3$ unknowns: the N_v independent variables of the state vector, the period T of the orbit and two phase shifts in y and z, which can be recast in the form of two phase velocities C_y and C_z using the period T. These extra variables are needed because the original problem of size N_v is under-determined due to translational space invariances (any phase-shifted solution is also a solution) and time invariance (any state $\boldsymbol{X}_0$ on a

periodic trajectory is a solution of equation (B 4)). An equal number of constraints must be imposed to lift the degeneracies and to make the numerical problem non-singular.

The Newton method solves equation (B 4) iteratively. Starting from an initial guess $\boldsymbol{X}_{g,0}$ of a point on a cycle, a succession of corrections $\delta\boldsymbol{X}_i$ to that guess are calculated from successive Jacobian inversions, producing a sequence of states $\boldsymbol{X}_{g,i}$ that should approach the desired solution if $\boldsymbol{X}_{g,0}$ is not too far from the solution. The extra constraints required to lift the translational and time degeneracies described above are

$$\left\langle \delta\boldsymbol{X}_i, \frac{\partial\boldsymbol{X}_{g,i}}{\partial y}\right\rangle = 0 \ , \tag{B 5}$$

$$\left\langle \delta\boldsymbol{X}_i, \frac{\partial\boldsymbol{X}_{g,i}}{\partial z}\right\rangle = 0 \ , \tag{B 6}$$

$$\langle \delta\boldsymbol{X}_i, \boldsymbol{F}(\boldsymbol{X}_{g,i})\rangle = 0 \ , \tag{B 7}$$

where the brackets denote a simple scalar product between state vectors in complex space. These constraints basically impose that the corrections performed by the solver be orthogonal to the directions of phase space along which the flow is invariant. However, the shear periodicity described in appendix A introduces an internal time $T_{SB} = L_y/SL_x$ in the system that breaks the continuous translational time invariance of the equations and turns it into a discrete one. To see this, consider the state $\boldsymbol{X}$ of the system at time $t = 0$. Because of the shearing of the basis of wavevectors on which the various fields are projected, it does not make sense to compare the Fourier coefficients for that state to those for different state at an arbitrary time t, because in general the wavevector basis at time t will be different from that at $t = 0$. The only times at which such a comparison is meaningful are the multiples of T_{SB} because for these times the sheared Fourier grid coincides with that at $t = 0$. In less technical terms, the time-periodicity of shear periodic boundary conditions in the x direction only makes it possible for periodic orbits of period that are multiples of T_{SB} to be present in the shearing box. Actually, because cycles require at least two reversals of the large-scale axisymmetric components of the fields triggered by successive nonlinear shearing wave interactions, they can only have periods multiple of $T_o = 2T_{SB}$ (Herault *et al.* 2011). In practice, a Newton search for a cycle whose estimated period is NT_o can be performed without imposing (B 7) by simply specifying the number N of successive T_o integrations.

Finally, enforcing the $\mathcal{A}_1$ symmetry described in appendix A.4 in the time integrations breaks the continuous translational invariances in space and notably eliminates relative periodic orbits. In that situation, the solver can converge to periodic orbits without imposing the phase constraints (B 5)-(B 6). We checked that convergence to the same periodic orbits is obtained whether the phase constraints are imposed or not. We also checked in several important cases that convergence to a given cycle with the Newton solver could be obtained independently of whether symmetries are imposed or not.

Appendix C. Numerical methods for homoclinic bifurcations

C.1. *Imaging unstable manifolds in the MRI dynamo problem*

A standard technique to analyse the dynamics in the neighbourhood of nonlinear invariant solutions is to look at the geometry of their unstable manifolds W^u using Poincaré return sections (Simó 1989). The method has for instance been used to analyse the nonlinear dynamics of the Kuramoto-Sivashinsky equation (Christiansen *et al.* 1997; Lan & Cvitanović 2008), and was recently introduced in the context of hydrodynamic plane Couette flow and pipe flow (Gibson *et al.* 2008, 2009; Halcrow *et al.* 2009; van Veen &

Kawahara 2011; Willis *et al.* 2013). Tracing an unstable manifold of a nonlinear periodic orbit is easier when the orbit has a single unstable eigenvalue, as happens to be the case in transitional ranges of Rm for the MRI dynamo cycles born out of SN_1 and SN_2, when the dynamics is limited to the $\mathcal{A}_1$ symmetric subspace. Assume we have a periodic orbit whose full phase space coordinates are denoted by $\boldsymbol{X}_e$. Close to $\boldsymbol{X}_e$, a good approximation of a point in the unstable manifold is given by the local tangent

$$\boldsymbol{X}_0 = \boldsymbol{X}_e + \varepsilon \boldsymbol{X}_u \ , \tag{C 1}$$

where $\boldsymbol{X}_u$ is the eigenvector associated with the unstable eigenvalue and ε is small enough for the tangent approximation of W^u at $\boldsymbol{X}_e$ to be valid (up to some reasonable accuracy). A full local segment of W^u can be approximated by sprinkling a large number of points with different ε on this tangent line. This set of points is then used as a set of initial conditions which can be integrated along the flow for as much time as desired. As W^u is invariant under the flow by definition, all image points resulting from the integration of the initial conditions in the initial segment also lie in W^u and can therefore be used to construct arbitrary long pieces of W^u further away from $\boldsymbol{X}_e$. Using successive crossings of dynamical trajectories with appropriate Poincaré sections in flows, or discrete iterations in the case of maps, and further projecting the dynamics on a low-dimensional subspace of the full phase space finally makes it possible to visualize W^u as a simple collection of points lying on a one-dimensional curve.

The numerical formulation of the problem makes it possible to analyse the nonlinear dynamics in terms of discrete-time map Φ_o which consists in integrating the fluid equations during T_o. Looking at the state of the system stroboscopically every T_o is equivalent to introducing a Poincaré section. In that stroboscopic representation, MRI dynamo cycles simply appear as nonlinear equilibrium points (hence the notation $\boldsymbol{X}_e$). Although looking at full snapshots of numerical simulations every T_o is not very informative, a low-dimensional projection of the dynamics can be introduced to uncover interesting behaviour. We use a two-dimensional projection on the large-scale axisymmetric magnetic field plane $(\overline{B}_{0x}, \overline{B}_{0y})$, equivalent to a streamwise vortex / streak projection in the hydrodynamic problem. Possible projection degeneracies can be lifted by introducing a third variable (e. g. another Fourier component of the spectral representation of the fields).

Let us summarize this technical description in order to make it a practical, useful recipe. To uncover the geometry of the unstable manifold W^u of a MRI dynamo cycle $\boldsymbol{X}_e$ with a single unstable eigenvalue, a preliminary requirement is to calculate the unstable eigenvector $\boldsymbol{X}_u$ of $\boldsymbol{X}_e$. This data is obtained from the SLEPc eigenvalue problem solver during the local stability analysis presented in §4. Using this vector and applying equation (C 1) for a large set of ε in a given range of small enough values, we generate a large set of initial conditions, or "initial segment" tangent to W^u at $\boldsymbol{X}_e$. Each initial condition in that set is then integrated in time with the SNOOPY code for a succession of periods T_o (typically 8 in the paper). After each T_o time integration (each corresponding to one Φ_o iteration), the results of all the simulations are projected on the two-dimensional plane $(\overline{B}_{0x}, \overline{B}_{0y})$ to obtain successive "image segments" of the initial one. As W^u is invariant under time integrations, these successive curved segments represent increasingly larger portions of the projection of W^u in the plane.

C.2. *Computation and continuation of homoclinic orbits*

Homoclinic orbits of fixed points of discrete-time maps are characterized by a unique symbolic sequence ("core") of finite intrinsic length (or transition time N_t). This sequence is preceded by an infinite repetition of the symbol associated with the fixed point and is followed by another infinite repetition of the same symbol. These head and tail sequences

represent exponential escape from the fixed point and exponential convergence back to it towards infinite times, while the core sequence of finite length represents the nonlinear excursion in the tangle, far away from the fixed point. A well-known map for which the zoology of homoclinic bifurcations and associated symbolic dynamics has been thoroughly studied is the Hénon map (Hénon 1976; Grassberger *et al.* 1989; Sterling *et al.* 1999).

C.2.1. *Capturing homoclinic orbits*

We only describe the homoclinic case, as the generalization to heteroclinic orbits is straightforward. To investigate homoclinic orbits of a MRI dynamo cycle (which we recall is a fixed point of the Φ_o map) in the associated tangle, we first construct the projection in the $(\overline{B}_{0x}, \overline{B}_{0y})$ plane of the unstable manifold W^u of the cycle using the technique described in §C.1. We typically construct 5 to 20 image segments in that case, depending on the desired approximation of the orbit. We then consider the fold of W^u approaching closest to the fixed point and identify the image point in the fold closest to it. We then track the pre-images of this point, back to its parent initial condition in the initial tangent segment. If the value of ε used to construct this particular initial condition according to equation (C 1) is sufficiently small so that the point can be considered to be part of the "head" sequence of a homoclinic orbit, the sequence of points resulting from successive T_o integrations of the initial condition already provides a good approximation of that orbit. However, as W^u is strongly stretched along itself close to the fixed point, a little change in ε can result in an important divergence of trajectories after just a few iterations. To obtain a reasonably accurate approximation of a specific homoclinic orbit, it is in general desirable to refine the initial condition. We use a bisection method on ε to minimize the distance between the last point of integration and the fixed point. Approximate orbits with an arbitrarily long head can be computed by using arbitrarily small initial segments. Approximate orbits with an arbitrarily long tail are obtained by increasing the target number of T_o integrations of the algorithm.

C.2.2. *Continuing homoclinic orbits in parameter space*

Assume that a homoclinic orbit $\mathcal{H}$ of an equilibrium point $\boldsymbol{X}_e$ of the map Φ_o has been approximately computed at a given Rm as a set of N successive states $\boldsymbol{H}_i$ ($i = 0, \cdots, N-1$) using the technique described above. $\boldsymbol{H}_0$ is the initial state closest to $\boldsymbol{X}_e$, $\boldsymbol{H}_1$ its image under the action of Φ_o, and so on. We also know from the calculation of $\mathcal{H}$ the parameter ε_0 from which $\boldsymbol{H}_0$ was computed.

To follow this orbit at a slightly different $Rm + \Delta Rm$, we first recompute $\boldsymbol{X}_e$ and its unstable eigenvector $\boldsymbol{X}_u$ at the target Rm using a standard continuation algorithm and stability solver, and construct a new perturbed state $\boldsymbol{H}_0^0$ using the same ε_0 as before. From this state, we perform N iterations of Φ_o of the map at the target Rm and obtain a new set of states $\boldsymbol{H}_i^0$. This set is not in general a good approximation of the homoclinic orbit at the new Rm. It usually increasingly diverges from $\mathcal{H}$ as the number of iterations of Φ_o increases. But we can use the difference between the two sets of states $\boldsymbol{H}_i^0$ and $\boldsymbol{H}_i$ to guess a new ε and better approximate the first point computed along the homoclinic orbit at the target Rm. We denote by F_N the function of ε which, for a given equilibrium $\boldsymbol{X}_e$ and corresponding unstable eigenvector $\boldsymbol{X}_u$ of Φ_o, gives the projection of the image of $\boldsymbol{X}_e + \varepsilon \boldsymbol{X}_u$ under the action of Φ_o^N on the $(\overline{B}_{0x}, \overline{B}_{0y})$ plane:

$$F_N : \mathbb{R} \to \mathbb{R}^2 \tag{C 2}$$

$$\varepsilon \mapsto \mathrm{P}\left[\Phi_o^N(\boldsymbol{X}_e + \varepsilon \boldsymbol{X}_u)\right] . \tag{C 3}$$

The two-dimensional projection P is not mandatory but makes the algorithm much faster than if we were to use the full state vector. We use a simple Newton algorithm to perform

the desired ε correction. Two possibilities must be considered. If the difference between $\boldsymbol{H}_i^0$ and $\boldsymbol{H}_i$ only becomes larger than a given threshold value in the tail sequence of the homoclinic orbit (i.e. after the "bursting" transition sequence of length N_t has been passed), say at iteration N_d, then a first Newton step is set up to converge to $\boldsymbol{H}_{N_d} = \boldsymbol{X}_e$ at the target Rm. In that case, the first Newton step reads

$$\varepsilon_1 = \varepsilon_0 - \tilde{J}_0 \, \mathrm{P} \left[\boldsymbol{H}_{N_d}^0 - \boldsymbol{X}_e \right] , \tag{C 4}$$

where $\tilde{J}_0 = ((J_0^T J_0)^{-1}) J_0^T$ is the pseudo-inverse of $J_0 = \left. \dfrac{dF_{N_d}}{d\varepsilon} \right|_{\varepsilon = \varepsilon_0}$.

ε_1 is used in a new prediction step to recompute an updated initial state $\boldsymbol{H}_0^1$. This state is integrated as before, producing a full new sequence $\boldsymbol{H}_i^1$. In general, one Newton step will not be enough to converge to the homoclinic solution at the target Rm, but the iteration of Φ_o at which the new sequence will diverge from the homoclinic orbit at the original Rm will be larger (and therefore still in the tail sequence). To take advantage of this, we increment N_d by one at each Newton iteration so that points ever further in the tail of the approximate orbit close in on $\boldsymbol{X}_e$. At step n, the correction step will read:

$$\varepsilon_n = \varepsilon_{n-1} - \tilde{J}_{n-1} \, \mathrm{P} \left[\boldsymbol{H}_{N_d+n-1}^{n-1} - \boldsymbol{X}_e \right] , \tag{C 5}$$

with $\tilde{J}_{n-1} = ((J_{n-1}^T J_{n-1})^{-1}) J_{n-1}^T$ the pseudo-inverse of $J_{n-1} = \left. \dfrac{dF_{N_d+n-1}}{d\varepsilon} \right|_{\varepsilon = \varepsilon_{n-1}}$.

In practice, the J_i Jacobians (which for the projection used are just two-dimensional vectors) are computed approximately using a first-order finite difference formula.

The algorithm must be slightly modified in the case of divergence in the head sequence (i.e. before the transition sequence of length N_t). In that case, we would like that all the points of the approximate orbit at the target Rm whose index is between N_d and the end of the transition sequence stay close to the corresponding points of the orbit $\mathcal{H}$ at the previous Rm. The first steps of the correction algorithm are modified according to:

$$\varepsilon_1 = \varepsilon_0 - \tilde{J}_0 \, \mathrm{P} \left[\boldsymbol{H}_{N_d}^0 - \boldsymbol{H}_{N_d} \right] , \tag{C 6}$$

$$\varepsilon_2 = \varepsilon_1 - \tilde{J}_1 \, \mathrm{P} \left[\boldsymbol{H}_{N_d+1}^1 - \boldsymbol{H}_{N_d+1} \right] , \tag{C 7}$$

and so on until the tail sequence of the orbit is reached. Once this is achieved, $\boldsymbol{X}_e$ becomes the target of the Newton algorithm and the same procedure as before is used.

This algorithm is somewhat empirical (there is no mathematical guarantee of convergence) but nevertheless give full satisfaction. Obviously, for such a strategy to work, ΔRm must be small enough so that $\mathcal{H}$ at the target Rm differs only weakly from $\mathcal{H}$ at the original Rm. A detailed examination of the results is necessary to check that the orbit found at the target Rm is a good numerical approximation of a homoclinic orbit, and that it is indeed the continuation of that obtained at the preceding Rm.

REFERENCES

ARMITAGE, P. J. 2010 *Astrophysics of Planet Formation*. Cambridge University Press.

AVILA, K., MOXEY, D., DE LOZAR, A., AVILA, M., BARKLEY, D. & HOF, B. 2011 The onset of turbulence in pipe flow. *Science* **333**, 192.

BALAY, SATISH, BROWN, JED, BUSCHELMAN, KRIS, GROPP, WILLIAM D., KAUSHIK, DINESH, KNEPLEY, MATTHEW G., MCINNES, LOIS CURFMAN, SMITH, BARRY F. & ZHANG, HONG 2011 PETSc Web page. http://www.mcs.anl.gov/petsc.

BALBUS, S. A. 2003 Enhanced angular momentum transport in accretion disks. *Annu. Rev. Astron. Astrophys.* **41**, 555.

BALBUS, S. A. & HAWLEY, J. F. 1991 A powerful local shear instability in weakly magnetized disks. I. Linear analysis. *Astrophys. J.* **376**, 214.

BALBUS, S. A. & HAWLEY, J. F. 1992 A powerful local shear instability in weakly magnetized disks. IV. Nonaxisymmetric perturbations. *Astrophys. J.* **400**, 610.

BALBUS, S. A. & HAWLEY, J. F. 1998 Instability, turbulence, and enhanced transport in accretion disks. *Rev. Mod. Phys.* **70**, 1.

BALBUS, S. A. & HENRI, P. 2008 On the magnetic Prandtl number behavior of accretion disks. *Astrophys. J.* **674**, 408.

BARKLEY, D. 2011 Simplifying the complexity of pipe flow. *Phys. Rev. E* **84**, 016309.

BIRKHOFF, G. D. 1935 Nouvelles recherches sur les systèmes dynamiques. *Mem. Pont. Acad. Sci. Nov. Lyn.* **1**, 85.

BODO, G., CATTANEO, F., FERRARI, A., MIGNONE, A. & ROSSI, P. 2011 Symmetries, scaling laws, and convergence in shearing-box simulations of magneto-rotational instability driven turbulence. *Astrophys. J.* **739**, 82.

BRANDENBURG, A. & DINTRANS, B. 2006 Nonaxisymmetric stability in the shearing sheet approximation. *Astron. Astrophys.* **450**, 437.

BRANDENBURG, A., NORDLUND, A., STEIN, R. F. & TORKELSSON, U. 1995 Dynamo-generated turbulence and large-scale magnetic fields in a Keplerian shear flow. *Astrophys. J.* **446**, 741.

CANUTO, C., HUSSAINI, M. Y., QUARTERONI, A. & ZANG, T. A. 1988 *Spectral Methods in Fluid Dynamics*. Springer.

CASCIOLA, C. M., GUALTIERI, P., BENZI, R. & PIVA, R. 2003 Scale-by-scale budget and similarity laws for shear turbulence. *J. Fluid Mech.* **476**, 105.

CHANDLER, G. J. & KERSWELL, R. R. 2013 Invariant recurrent solutions embedded in a turbulent two-dimensional Kolmogorov flow. *J. Fluid Mech.* **722**, 554.

CHANDRASEKHAR, S. 1960 *Proc. Natl. Acad. Sci.* **46**, 253.

CHILDRESS, S. & GILBERT, A. D. 1995 *Stretch, Twist, Fold. The Fast Dynamo*. Springer-Verlag.

CHRISTIANSEN, F., CVITANOVIĆ, P. & PUTKARADZE, V. 1997 Spatiotemporal chaos in terms of unstable recurrent patterns. *Nonlinearity* **10**, 55.

CLINE, K. S., BRUMMELL, N. H. & CATTANEO, F. 2003 Dynamo action driven by shear and magnetic buoyancy. *Astrophys. J.* **599**, 1449.

COLLINS, C., KATZ, N., WALLACE, J., JARA-ALMONTE, J., REESE, I., ZWEIBEL, E. & FOREST, C. B. 2012 Stirring unmagnetized plasma. *Phys. Rev. Lett.* **108**, 115001.

CVITANOVIĆ, P. 1992 Periodic orbit theory in classical and quantum mechanics. *Chaos* **2**, 1.

CVITANOVIĆ, P. & GIBSON, J. F. 2010 Geometry of the turbulence in wall-bounded shear flows: periodic orbits. *Physica Scripta* **142**, 014007.

DARBYSHIRE, A. G. & MULLIN, T. 1995 Transition to turbulence in constant-mass-flux pipe flow. *J. Fluid Mech.* **289**, 83.

DAUCHOT, O. & DAVIAUD, F. 1995a Finite amplitude perturbation and spots growth mechanism in plane Couette flow. *Phys. Fluids* **7**, 335.

DAUCHOT, O. & DAVIAUD, F. 1995b Streamwise vortices in plane Couette flow. *Phys. Fluids* **7**, 901.

DAVIES, C. R. & HUGHES, D. W. 2011 The mean electromotive force resulting from magnetic buoyancy instability. *Astrophys. J.* **727**, 112.

DAVIS, S. W., STONE, J. M. & PESSAH, M. E. 2010 Sustained magnetorotational turbulence in local simulations of stratified disks with zero net magnetic flux. *Astrophys. J.* **713**, 52.

DE LOZAR, A., MELLIBOVSKY, F., AVILA, M. & HOF, B. 2012 Edge state in pipe flow experiments. *Phys. Rev. Lett.* **108**, 214502.

DING, M., GREBOGI, C., OTT, E. & YORKE, J. A. 1990 Transition to chaotic scattering. *Phys. Rev. A* **42**, 7025.

DUGUET, Y., PRINGLE, C. C. T. & KERSWELL, R. R. 2008a Relative periodic orbits in transitional pipe flow. *Phys. Fluids* **20**, 114102.

DUGUET, Y., WILLIS, A. P. & KERSWELL, R. R. 2008b Transition in pipe flow: the saddle structure on the boundary of turbulence. *J. Fluid Mech.* **613**, 255.

ECKHARDT, B. 2009 Introduction. Turbulence transition in pipe flow: 125th anniversary of the publication of Reynolds' paper. *Proc. R. Soc. Lond. Series A* **367**, 449.

Eckhardt, B., Schneider, T. M., Hof, B. & Westerweel, J. 2007 Turbulence transition in pipe flow. *Annu. Rev. Fluid Mech.* **39**, 447.

Faisst, H. & Eckhardt, B. 2003 Traveling waves in pipe flow. *Phys. Rev. Lett.* **91**, 224502.

Faisst, H. & Eckhardt, B. 2004 Sensitive dependence on initial conditions in transition to turbulence in pipe flow. *J. Fluid Mech.* **504**, 343.

Feigenbaum, M. J. 1978 Quantitative universality for a class of nonlinear transformations. *J. Stat. Phys.* **19**, 25.

Frank, J., King, A. & Raine, D. J. 2002 *Accretion Power in Astrophysics: Third Edition*. Cambridge University Press.

Fromang, S. & Papaloizou, J. C. B. 2007 MHD simulations of the magnetorotational instability in a shearing box with zero net flux. I. The issue of convergence. *Astron. Astrophys.* **476**, 1113.

Fromang, S., Papaloizou, J. C. B., Lesur, G. & Heinemann, T. 2007 MHD simulations of the magnetorotational instability in a shearing box with zero net flux. II. The effect of transport coefficients. *Astron. Astrophys.* **476**, 1123.

Gallet, B., Herault, J., Laroche, C., Pétrélis, F & Fauve, S. 2012 Reversals of large-scale fields generated over a turbulent background. *Geophys. Astrophys. Fluid Dyn.* **106**, 468.

Gavrilov, N. & Shil'nikov, L. 1972 On the three dimensional dynamical systems close to a system with a structurally unstable homoclinic curve, i. *Math. USSR Sbornik* **17**, 467.

Gibson, J. F., Halcrow, J. & Cvitanović, P. 2008 Visualizing the geometry of state space in plane Couette flow. *J. Fluid Mech.* **611**, 107.

Gibson, J. F., Halcrow, J. & Cvitanović, P. 2009 Equilibrium and travelling-wave solutions of plane Couette flow. *J. Fluid Mech.* **638**, 243.

Gissinger, C. 2012 A new deterministic model for chaotic reversals. *Eur. Phys. J. B* **85**, 137.

Goldreich, P. & Lynden-Bell, D. 1965 II. Spiral arms as sheared gravitational instabilities. *Mon. Not. R. Astron. Soc.* **130**, 125.

Goswami, B. K. & Basu, S. 2002 Self-similar organization of Gavrilov-Silnikov-Newhouse sinks. *Phys. Rev. E* **65**, 036210.

Grassberger, P., Kantz, H. & Moenig, U. 1989 On the symbolic dynamics of the Hénon map. *J. Phys. A* **22**, 5217.

Grebogi, C., Ott, E. & Yorke, J. A. 1982 Chaotic attractors in crisis. *Phys. Rev. Lett.* **48**, 1507.

Grebogi, C., Ott, E. & Yorke, J. A. 1983 Crises, sudden changes in chaotic attractors, and transient chaos. *Physica D* **7**, 181.

Grebogi, C., Ott, E. & Yorke, J. A. 1987 Basin boundary metamorphoses: Changes in accessible boundary orbits. *Physica D* **24**, 243.

Gressel, O. 2010 A mean-field approach to the propagation of field patterns in stratified magnetorotational turbulence. *Mon. Not. R. Astron. Soc.* **405**, 41.

Grossmann, S. 2000 The onset of shear flow turbulence. *Rev. Mod. Phys.* **72**, 603.

Gualtieri, P., Casciola, C. M., Benzi, R., Amati, G. & Piva, R. 2002 Scaling laws and intermittency in homogeneous shear flow. *Phys. Fluids* **14**, 583.

Halcrow, J., Gibson, J. F., Cvitanović, P. & Viswanath, D. 2009 Heteroclinic connections in plane Couette flow. *J. Fluid Mech.* **621**, 365.

Hamilton, J. M., Kim, J. & Waleffe, F. 1995 Regeneration mechanisms of near-wall turbulence structures. *J. Fluid Mech.* **287**, 317.

Hartmann, L. 2009 *Accretion Processes in Star Formation: Second Edition*. Cambridge University Press.

Hawley, J. F. & Balbus, S. A. 1991 A powerful local shear instability in weakly magnetized disks. II. Nonlinear evolution. *Astrophys. J.* **376**, 223.

Hawley, J. F., Gammie, C. F. & Balbus, S. A. 1995 Local three-dimensional magnetohydrodynamic simulations of accretion disks. *Astrophys. J.* **440**, 742.

Hawley, J. F., Gammie, C. F. & Balbus, S. A. 1996 Local three-dimensional simulations of an accretion disk hydromagnetic dynamo. *Astrophys. J.* **464**, 690.

Hénon, M. 1976 A two-dimensional mapping with a strange attractor. *Commun. Math. Phys.* **50**, 69.

Herault, J., Rincon, F., Cossu, C., Lesur, G., Ogilvie, G. I. & Longaretti, P.-Y.

2011 Periodic magnetorotational dynamo action as a prototype of nonlinear magnetic-field generation in shear flows. *Phys. Rev. E* **84**, 036321.

HERNANDEZ, VICENTE, ROMAN, JOSE E. & VIDAL, VICENTE 2005 SLEPc: A scalable and flexible toolkit for the solution of eigenvalue problems. *ACM Transactions on Mathematical Software* **31**, 351.

HOF, B., DE LOZAR, A., KUIK, D. J. & WESTERWEEL, J. 2008 Repeller or attractor? Selecting the dynamical model for the onset of turbulence in pipe flow. *Phys. Rev. Lett.* **101**, 214501.

HOF, B., JUEL, A. & MULLIN, T. 2003 Scaling of the turbulence transition threshold in a pipe. *Phys. Rev. Lett.* **91**, 244502.

HOF, B., VAN DOORNE, C. W. H., WESTERWEEL, J., NIEUWSTADT, F. T. M., FAISST, H., ECKHARDT, B., WEDIN, H., KERSWELL, R. R. & WALEFFE, F. 2004 Experimental observation of nonlinear traveling waves in turbulent pipe flow. *Science* **305**, 1594.

HOF, B., WESTERWEEL, J., SCHNEIDER, T. M. & ECKHARDT, B. 2006 Finite lifetime of turbulence in shear flows. *Nature* **443**, 59.

HWANG, Y. & COSSU, C. 2010 Self-sustained process at large scales in turbulent channel flow. *Phys. Rev. Lett.* **105**, 044505.

HWANG, Y. & COSSU, C. 2011 Self-sustained processes in the logarithmic layer of turbulent channel flows. *Phys. Fluids* **23**, 061702.

ITANO, T. & TOH, S. 2001 The dynamics of bursting process in wall turbulence. *J. Phys. Soc. Jpn.* **70**, 703.

KÄPYLÄ, P. J. & KORPI, M. J. 2011 Magnetorotational instability driven dynamos at low magnetic Prandtl numbers. *Mon. Not. R. Astron. Soc.* **413**, 901.

KAWAHARA, G. & KIDA, S. 2001 Periodic motion embedded in plane Couette turbulence: regeneration cycle and burst. *J. Fluid Mech.* **449**, 291.

KAWAHARA, G., UHLMANN, M. & VAN VEEN, L. 2012 The significance of simple invariant solutions in turbulent flows. *Annu. Rev. Fluid Mech.* **44**, 203.

KERSWELL, R. R. 2005 Recent progress in understanding the transition to turbulence in a pipe. *Nonlinearity* **18**, 17.

KERSWELL, R. R. & TUTTY, O. R. 2007 Recurrence of travelling waves in transitional pipe flow. *J. Fluid Mech.* **584**, 69.

KIM, L. & MOEHLIS, J. 2008 Characterizing the edge of chaos for a shear flow model. *Phys. Rev. E* **78**, 036315.

KNOBLOCH, E. 1985 The stability of non-separable barotropic and baroclinic shear flows. *Astrophys. Space Sci.* **116**, 149.

KNOBLOCH, E. & MOORE, D. R. 1986 Transition to chaos in two-dimensional double-diffusive convection. *J. Fluid Mech.* **166**, 409.

KNOBLOCH, E. & WEISS, N. O. 1981 Bifurcations in a model of double-diffusive convection. *Phys. Lett. A* **85**, 127.

KORYCANSKY, D. G. 1992 Growth and decay of disturbances in stratified shear flow in a rotating frame. *Astrophys. J.* **399**, 176.

KREILOS, T. & ECKHARDT, B. 2012 Periodic orbits near the onset of chaos in plane couette flow. *Chaos* **22**, 047505.

LAN, Y. & CVITANOVIĆ, P. 2008 Unstable recurrent patterns in Kuramoto-Sivashinsky dynamics. *Phys. Rev. E* **78**, 026208.

LANDAHL, M. T. 1980 A note on an algebraic instability of inviscid parallel shear flows. *J. Fluid Mech.* **98**, 243.

LEBOVITZ, N. R. 2009 Shear-flow transition: the basin boundary. *Nonlinearity* **22**, 2645.

LEBOVITZ, N. R. 2012 Boundary collapse in models of shear-flow transition. *Communications in Nonlinear Science and Numerical Simulation* **17**, 2095.

LESUR, G. & LONGARETTI, P.-Y. 2005 On the relevance of subcritical hydrodynamic turbulence to accretion disk transport. *Astron. Astrophys.* **444**, 25.

LESUR, G. & LONGARETTI, P.-Y. 2007 Impact of dimensionless numbers on the efficiency of magnetorotational instability induced turbulent transport. *Mon. Not. R. Astron. Soc.* **378**, 1471.

LESUR, G. & OGILVIE, G. I. 2008*a* Localized magnetorotational instability and its role in the accretion disc dynamo. *Mon. Not. R. Astron. Soc.* **391**, 1437.

Lesur, G. & Ogilvie, G. I. 2008*b* On self-sustained dynamo cycles in accretion discs. *Astron. Astrophys.* **488**, 451.

Lin, D. N. C. & Papaloizou, J. C. B. 1996 Theory of accretion disks II: application to observed systems. *Annu. Rev. Astron. Astrophys.* **34**, 703.

Longaretti, P.-Y. & Lesur, G. 2010 MRI-driven turbulent transport: the role of dissipation, channel modes and their parasites. *Astron. Astrophys.* **516**, 51.

Lord Kelvin 1887 Stability of fluid motion - rectilineal motion of viscous fluid between two parallel planes. *Phil. Mag.* **24**, 188.

Lynden-Bell, D. & Pringle, J. E. 1974 The evolution of viscous discs and the origin of the nebular variables. *Mon. Not. R. Astron. Soc.* **168**, 603.

Manneville, P. 2009 Spatiotemporal perspective on the decay of turbulence in wall-bounded flows. *Phys. Rev. E* **79**, 025301.

Mellibovsky, F. & Eckhardt, B. 2011 Takens-Bogdanov bifurcation of travelling-wave solutions in pipe flow. *J. Fluid Mech.* **670**, 96.

Mellibovsky, F. & Eckhardt, B. 2012 From travelling waves to mild chaos: a supercritical bifurcation cascade in pipe flow. *J. Fluid Mech.* **709**, 149.

Mellibovsky, F., Meseguer, A., Schneider, T. M. & Eckhardt, B. 2009 Transition in localized pipe flow turbulence. *Phys. Rev. Lett.* **103**, 054502.

Miesch, M. S., Gilman, P. A. & Dikpati, M. 2007 Nonlinear evolution of global magnetoshear instabilities in a three-dimensional thin-shell model of the solar tachocline. *ApJ. Supp. Ser.* **168**, 337.

Moehlis, J., Eckhardt, B. & Faisst, H. 2004*a* Fractal lifetimes in the transition to turbulence. *Chaos* **14**, 11.

Moehlis, J., Faisst, H. & Eckhardt, B. 2004*b* A low-dimensional model for turbulent shear flows. *New Journal of Physics* **6**, 56.

Moehlis, J., Faisst, H. & Eckhardt, B. 2005 Periodic orbits and chaotic sets in a low-dimensional model for shear flows. *SIAM J. Appl. Dyn. Syst.* **4**, 352.

Moehlis, J., Smith, T. R., Holmes, P. & Faisst, H. 2002 Models for turbulent plane Couette flow using the proper orthogonal decomposition. *Phys. Fluids* **14**, 2493.

Moffatt, H. K. 1977 *Magnetic field generation in electrically conducting fluids*. Cambridge University Press.

Monchaux, R., Berhanu, M., Aumaitre, S., Chiffaudel, A., Daviaud, F., Dubrulle, B., Ravelet, F., Fauve, S., Mordant, N., Petrelis, F., Bourgoin, M., Odier, P., Pinton, J.-F., Plihon, N. & Volk, R. 2009 The Von Kármán Sodium experiment: turbulent dynamical dynamos. *Phys. Fluids* **21**, 035108.

Moore, D. R., Toomre, J., Knobloch, E. & Weiss, N. O. 1983 Period doubling and chaos in partial differential equations for thermosolutal convection. *Nature* **303**, 663.

Moxey, D. & Barkley, D. 2010 Distinct large-scale turbulent-laminar states in transitional pipe flow. *Proc. Nat. Acad. Sci.* **107** (18), 8091.

Nagata, M. 1986 Bifurcations in Couette flow between almost corotating cylinders. *J. Fluid Mech.* **169**, 229.

Nagata, M. 1990 Three-dimensional finite-amplitude solutions in plane Couette flow: bifurcation from infinity. *J. Fluid Mech.* **217**, 519.

Newhouse, S. E. 1979 The abundance of wild hyperbolic sets and nonsmooth stable sets for diffeomorphisms. *Publ. Math. I.H.E.S.* **50**, 101.

Ogilvie, G. I. & Pringle, J. E. 1996 The non-axisymmetric instability of a cylindrical shear flow containing an azimuthal magnetic field. *Mon. Not. R. Astron. Soc.* **279**, 152.

Oishi, J. S. & Mac Low, M.-M. 2011 Magnetorotational turbulence transports angular momentum in stratified disks with low magnetic Prandtl number but magnetic Reynolds number above a critical value. *Astrophys. J.* **740**, 18.

Orr, W. M. 1907 The stability or instability of the steady motions of a perfect liquid and of a viscous liquid. part I: a perfect liquid. *Proc. R. Irish Acad. A.* **27**, 9.

Ott, E. 2002 *Chaos in dynamical systems*. Cambridge University Press.

Palis, J. & Takens, F. 1993 *Hyperbolicity and sensitive chaotic dynamics at homoclinic bifurcations*. Cambridge University Press.

Papaloizou, J. C. B. & Lin, D. N. C. 1995 Theory of accretion disks I: angular momentum transport processes. *Annu. Rev. Astron. Astrophys.* **33**, 505.

Peixinho, J. & Mullin, T. 2006 Decay of turbulence in pipe flow. *Phys. Rev. Lett.* **96**, 094501.

Pomeau, Y. 1986 Front motion, metastability and subcritical bifurcations in hydrodynamics. *Physica D* **23**, 3.

Pringle, C. C. T., Duguet, Y. & Kerswell, R. R. 2009 Highly symmetric travelling waves in pipe flow. *Phil. Trans. R. Soc. Lond. A* **367**, 457.

Pringle, C. C. T. & Kerswell, R. R. 2007 Asymmetric, helical, and mirror-symmetric traveling waves in pipe flow. *Phys. Rev. Lett.* **99**, 074502.

Pringle, J. E. 1981 Accretion discs in astrophysics. *Annu. Rev. Astron. Astrophys.* **19**, 137.

Pumir, A. 1996 Turbulence in homogeneous shear flows. *Phys. Fluids* **8**, 3112.

Rempel, E. L., Lesur, G. & Proctor, M. R. E. 2010 Supertransient magnetohydrodynamic turbulence in Keplerian shear flows. *Phys. Rev. Lett.* **105**, 044501.

Reynolds, O. 1883 An experimental investigation of the circumstances which determine whether the motion of water shall be direct of sinuous and of the law of resistance in parallel channels. *Phil. Trans. R. Soc.* **174**, 935.

Rincon, F., Ogilvie, G. I. & Proctor, M. R. E. 2007 Self-sustaining nonlinear dynamo process in Keplerian shear flows. *Phys. Rev. Lett.* **98**, 254502.

Rincon, F., Ogilvie, G. I., Proctor, M. R. E. & Cossu, C. 2008 Subcritical dynamos in shear flows. *Astron. Nachr.* **329**, 750.

Robinson, C. 1983 Bifurcation to infinitely many sinks. *Commun. Math. Phys.* **90**, 433.

Schmid, P. J. & Henningson, D. S. 2000 *Stability and transition in shear flows*. Springer-Verlag, Berlin.

Schmiegel, A. 1997 Fractal stability border in plane couette Flow. *Phys. Rev. Lett.* **79**, 5250.

Schneider, T., Eckhardt, B. & Yorke, J. A. 2006 Edge of chaos in pipe flow. *Chaos* **16**, 041103.

Schneider, T., Eckhardt, B. & Yorke, J. A. 2007a Turbulence transition and the edge of chaos in pipe flow. *Phys. Rev. Lett.* **99**, 034502.

Schneider, T. M. & Eckhardt, B. 2008 Lifetime statistics in transitional pipe flow. *Phys. Rev. E* **78**, 046310.

Schneider, T. M., Eckhardt, B. & Vollmer, J. 2007b Statistical analysis of coherent structures in transitional pipe flow. *Phys. Rev. E* **75**, 066313.

Schneider, T. M., Gibson, J. F., Lagha, M., de Lillo, F. & Eckhardt, B. 2008 Laminar-turbulent boundary in plane Couette flow. *Phys. Rev. E* **78**, 037301.

Simó, C. 1989 In *Les Méthodes Modernes de la Mécanique Céleste (Goutelas '89)* (ed. D. Benest & C. Froeschlé), p. 285. Editions Frontières, Gif-sur-Yvette.

Simon, J. B., Beckwith, K. & Armitage, P. J. 2012 Emergent mesoscale phenomena in magnetized accretion disc turbulence. *Mon. Not. R. Astron. Soc.* **422**, 2685.

Simon, J. B., Hawley, J. F. & Beckwith, K. 2011 Resistivity-driven state changes in vertically stratified accretion disks. *Astrophys. J.* **730**, 94.

Skufca, J. D., Yorke, J. A. & Eckhardt, B. 2006 Edge of chaos in a parallel shear flow. *Phys. Rev. Lett.* **96**, 174101.

Smale, S. 1967 Differentiable dynamical systems. *Bull. Amer. Math. Soc.* **73**, 747.

Sparrow, C. 1982 *The Lorenz Equations: Bifurcation, Chaos and Strange Attractors*, Appl. Math. Sci., vol. 41. Springer-Verlag.

Spruit, H. C. 2002 Dynamo action by differential rotation in a stably stratified stellar interior. *Astron. Astrophys.* **381**, 923.

Steenbeck, M., Krause, F. & Rädler, K.-H. 1966 Berechnung der mittleren LORENTZ-Feldstärke $\overline{v \times B}$ für ein elektrisch leitendes Medium in turbulenter, durch CORIOLIS-Kräfte beeinflußter Bewegung. *Z. Naturforschung Teil A* **21**, 369.

Sterling, D., Dullin, H. R. & Meiss, J. D. 1999 Homoclinic bifurcations for the Hénon map. *Physica D* **134**, 153.

Stone, J. M., Hawley, J. F., Gammie, C. F. & Balbus, S. A. 1996 Three-dimensional magnetohydrodynamical simulations of vertically stratified accretion disks. *Astrophys. J.* **463**, 656.

Swift, J. W. & Wiesenfeld, K. 1984 Suppression of period doubling in symmetric systems. *Phys. Rev. Lett.* **52**, 705.

Terquem, C. & Papaloizou, J. C. B. 1996 On the stability of an accretion disc containing a toroidal magnetic field. *Mon. Not. R. Astron. Soc.* **279**, 767.

Tobias, S. M., Cattaneo, F. & Brummell, N. H. 2011 On the generation of organized magnetic fields. *Astrophys. J.* **728**, 153.

Umurhan, O. M. & Regev, O. 2004 Hydrodynamic stability of rotationally supported flows: Linear and nonlinear 2D shearing box results. *Astron. Astrophys.* **427**, 855.

van Veen, L. & Kawahara, G. 2011 Homoclinic tangle on the edge of shear turbulence. *Phys. Rev. Lett.* **107**, 114501.

Velikhov, E. P. 1959 Stability of an ideally conducting liquid flowing between cylinders rotating in a magnetic field. *Sov. Phys. JETP* **36**, 1398.

Viswanath, D. 2007 Recurrent motions within plane Couette turbulence. *J. Fluid Mech.* **580**, 339.

Vollmer, J., Schneider, T. & Eckhardt, B. 2009 Basin boundary, edge of chaos and edge state in a two dimensional model. *New Journal of Physics* **11**, 013040.

Waleffe, F. 1995*a* Hydrodynamic stability and turbulence: beyond transients to a self-sustaining process. *Studies in Applied Math.* **95**, 319.

Waleffe, F. 1995*b* Transition in shear flows. Nonlinear normality versus non-normal linearity. *Phys. Fluids* **7**, 3060.

Waleffe, F. 1997 On a self-sustaining process in shear flows. *Phys. Fluids* **9**, 883.

Waleffe, F. 1998 Three-dimensional coherent states in plane shear flows. *Phys. Rev. Lett.* **81**, 4140.

Waleffe, F. 2001 Exact coherent structures in channel flow. *J. Fluid Mech.* **435**, 93.

Waleffe, F. 2003 Homotopy of exact coherent structures in plane shear flows. *Phys. Fluids* **15**, 1517.

Wang, J., Gibson, J. & Waleffe, F. 2007 Lower branch coherent states in shear flows: transition and control. *Phys. Rev. Lett.* **98**, 204501.

Wedin, H. & Kerswell, R. R. 2004 Exact coherent structures in pipe flow: travelling wave solutions. *J. Fluid Mech.* **508**, 333.

Willis, A. P., Cvitanović, P. & Avila, M. 2013 Revealing the state space of turbulent pipe flow by symmetry reduction. *J. Fluid Mech.* **721**, 514.

Willis, A. P. & Kerswell, R. R. 2007 Critical behavior in the relaminarization of localized turbulence in pipe flow. *Phys. Rev. Lett.* **98**, 014501.

Willis, A. P. & Kerswell, R. R. 2009 Turbulent dynamics of pipe flow captured in a reduced model: puff relaminarization and localized 'edge' states. *J. Fluid Mech.* **619**, 213.

Yorke, J. A. & Alligood, T. 1983 Period doubling cascades of attractors: a prerequisite for horseshoes. *Bull. Amer. Math. Soc.* **9**, 319.

Zel'dovich, Y. B., Ruzmaikin, A. A., Molchanov, S. A. & Sokoloff, D. D. 1984 Kinematic dynamo problem in a linear velocity field. *J. Fluid Mech.* **144**, 1.